

Highlights

Hydrocarbon complexity and photochemical shielding of prebiotic feedstock molecules in exoplanet atmospheres

Marrick Braam, Ellery Gopaoco, Shang-Min Tsai, Gergely Friss, Paul I. Palmer, Paul B. Rimmer, Skyla B. White

- The production of prebiotic feedstock molecules varies with exoplanet atmospheric environments and chemical networks.
- Hydrocarbon shielding significantly affects prebiotic chemical processes.
- Key pathways identified to guide experimental rate measurements, chemical network reconciliation, and reduction strategies for complex climate–chemistry models.
- Crucial role of photochemical network structure and kinetics in understanding prebiotic feedstock molecules in exoplanet atmospheres.

Hydrocarbon complexity and photochemical shielding of prebiotic feedstock molecules in exoplanet atmospheres

Marrick Braam^{a,*}, Ellery Gopaoco^b, Shang-Min Tsai^{c,d}, Gergely Friss^{e,b}, Paul I. Palmer^{f,b}, Paul B. Rimmer^g and Skyla B. White^g

^aCenter for Space and Habitability, University of Bern, Gesellschaftsstrasse 6, Bern, 3012, Switzerland

^bCentre for Exoplanet Science, University of Edinburgh, Edinburgh, EH9 3FD, UK

^cDepartment of Earth and Planetary Sciences, University of California Riverside, Riverside, CA, USA

^dInstitute of Astronomy & Astrophysics, Academia Sinica, Taipei 10617, Taiwan, Taipei, 10617, Taiwan

^eSchool of Physics and Astronomy, University of Edinburgh, Edinburgh, EH9 3FD, UK

^fSchool of GeoSciences, University of Edinburgh, Edinburgh, EH9 3FF, UK

^gCavendish Laboratory, University of Cambridge, JJ Thomson Avenue, Cambridge, CB3 0HE, UK

ARTICLE INFO

Keywords:

Exoplanet atmospheres
Exoplanet atmospheric composition
Prebiotic astrochemistry

ABSTRACT

The potential of prebiotic chemistry to initiate and propagate on an exoplanet fundamentally depends on whether the atmospheric physical and chemical conditions can facilitate the production of prebiotic feedstock molecules. Photochemical simulations of exoplanet atmospheres can be used to explore this potential atmospheric synthesis, but require a comprehensive chemical network for the conditions considered. We present the implementation of the Consistent Reduced Atmospheric Hybrid Chemical Network with Oxygen extension (CRAHCN-O), constructed to simulate the formation of feedstock molecules such as hydrogen cyanide (HCN), formaldehyde (H₂CO), and simple hydrocarbons, into the VULCAN photochemical kinetics code. We investigate the photochemical production of feedstock molecules driven by M-star radiation and compare these to predictions by the N-C-H-O network in VULCAN, for N₂-dominated atmospheres with C/O ratios between 0.5–1.5 from CO₂ and CH₄ abundances. Predicted abundances are similar for C/O=0.5 in the absence of CH₄. As soon as CH₄ is included (i.e., for C/O>0.5), the abundance profiles diverge in the photochemical regions. By analysing the attenuation of UV radiation, we find that hydrocarbon photochemical shielding causes the diverging profiles. CRAHCN-O accumulates ethane (C₂H₆), while sinks to higher-order hydrocarbons in N-C-H-O accumulate C₄H₃ (the 1-butene-3-yne-1-yl radical) and C₃H₄ (allene). Importantly, C₂H₆ is photochemically active whereas C₄H₃ and C₃H₄ are assumed inactive. With mixing ratios up to a few percent in CRAHCN-O, C₂H₆ shields CH₄ and CO₂ from photodissociation. Therefore, these species survive to lower pressures, in turn weakening the destruction of HCN and H₂CO. Maximum HCN mixing ratios reach 1000 ppm for the highest CH₄ abundances with CRAHCN-O compared to only 3 ppm with N-C-H-O. Other feedstock molecules like cyanoacetylene (HC₃N) and acetylene (C₂H₂) form more efficiently in N-C-H-O. The shielding mechanism and its impact on feedstock molecules persist for radiation from distinct M-star types. We present the key pathways to feedstock molecules, along with photochemical cycles and net reactions to hydrocarbons for each network. These findings can be used to prioritise experimental rate coefficient determination, to reconcile network differences, and to develop more complex climate-chemistry modeling. The results demonstrate the crucial role of chemical kinetics in understanding prebiotic chemistry in exoplanet atmospheres, including important considerations for the construction and applicability of chemical networks.

1. Introduction

Evidence for the first appearance of life on Earth dates back to 3.7 Ga, while the planet may have been habitable as early as 4.3 Ga (Schopf, 2006; Zahnle et al., 2007; Pearce et al., 2018; Catling & Zahnle, 2020). Early studies on the origin of life proposed that the complex organic chemistry required for its emergence would have necessitated a more reducing environment than Earth's present oxidising atmosphere (Haldane, 1929; Oparin, 1938). This idea formed the

*Corresponding author

✉ marrick.braam@unibe.ch (M. Braam)

ORCID(s): <https://orcid.org/0000-0002-9076-2361> (M. Braam); <https://orcid.org/0000-0002-8163-4608> (S. Tsai);

<https://orcid.org/0009-0008-5099-5698> (G. Friss); <https://orcid.org/0000-0002-1487-0969> (P.I. Palmer);

<https://orcid.org/0000-0002-7180-081X> (P.B. Rimmer); <https://orcid.org/0009-0005-0027-7426> (S.B. White)

basis for the Miller-Urey experiments (Miller, 1953), which demonstrated that a reducing gas mixture (H_2 , H_2O , CH_4 , and NH_3) could yield simple prebiotic molecules such as hydrogen cyanide (HCN) and formaldehyde (H_2CO), when subjected to electrical discharges. In aqueous solution, the simple feedstock molecules can synthesise the building blocks of life (see also Bada, 2013). Candidate environments to facilitate this synthesis on Early Earth include shallow ponds undergoing wet-dry cycles that concentrate feedstock molecules (e.g., Pearce et al., 2017; Damer & Deamer, 2020), given sufficient atmospheric production and delivery, such as rainout and gravitational settling. Other theories for the origin of life include exogenous delivery of prebiotic feedstock molecules (e.g., Chyba & Sagan, 1992) and hydrothermal vent synthesis of prebiotic molecules (Shock, 1990). The increasing diversity of known rocky exoplanets (e.g., in terms of irradiation by and orbital distance from the host star) encourages investigations of the atmospheric synthesis of feedstock molecules in these exoplanet environments (Ranjan & Sasselov, 2016; Rimmer et al., 2018). Therefore, understanding the atmospheric chemical and physical conditions that allow for the formation of feedstock molecules and facilitate subsequent increasing chemical complexity is central to exploring the origin of life on Earth and beyond.

Several feedstock molecules are crucial for the synthesis of complex biomolecules. HCN can produce amino acids in the presence of NH_3 and aldehydes via Strecker synthesis (Strecker, 1854). Furthermore, HCN can directly polymerise into nucleobases such as adenine and guanine (Ferris & Orgel, 1966; Sanchez et al., 1967; Bada, 2004) and is a key driver of the cyanosulfidic protometabolism, which has shown that RNA, protein, and lipid precursors can emerge simultaneously (Ritson & Sutherland, 2012; Patel et al., 2015; Xu et al., 2018; Rimmer et al., 2018). Cyanoacetylene (HC_3N) is another simple nitrile that plays an essential role in the synthesis of RNA precursors (Powner et al., 2007, 2009). H_2CO is a simple aldehyde that can aid Strecker synthesis and forms sugars like ribose, which forms the backbone of RNA (Butlerow, 1861; Cleaves, 2008; Kim et al., 2011; Benner et al., 2020). Lastly, acetylene (C_2H_2) and ethylene (C_2H_4) can form long hydrocarbon chains, potentially important constituents of primitive cell membranes (Balucani, 2009; Ruiz-Mirazo et al., 2014). On Titan, increasingly complex organic molecules aggregate to non-volatile solids or hazes that can produce amino acids and nucleobases through hydrolysis (e.g., Khare et al., 1986; Poch et al., 2012; Hörst et al., 2012). Therefore, the formation of HCN, HC_3N , H_2CO , and hydrocarbons such as C_2H_2 and C_2H_4 in representative atmospheric conditions gives insights into the prebiotic potential of the planet in question.

However, the formation of any of these molecules will strongly depend on the environmental conditions (e.g., Bada & Lazcano, 2002), as also shown by the Miller-Urey experiments (Miller & Urey, 1959). Many experiments of atmospheric prebiotic synthesis followed, also considering a background atmosphere dominated by N_2 and CO_2 (e.g., Miller & Schlesinger, 1983; Miyakawa et al., 2002; Cleaves et al., 2008). The experimental studies were complemented by photochemical models of prebiotic synthesis, simulating the photochemical balance of feedstock molecules in a single atmospheric column for the Early Earth (Zahnle, 1986; Tian et al., 2011; Airapetian et al., 2016; Pearce et al., 2022b), Titan (Yung et al., 1984; Lavvas et al., 2008; Krasnopolsky, 2009; Hébrard et al., 2012; Dobrijevic et al., 2016; Loison et al., 2015; Willacy et al., 2016; Vuitton et al., 2019; Pearce et al., 2020b), and rocky exoplanets (Rimmer et al., 2018; Rimmer & Rugheimer, 2019). An important outcome of these is the clear link between HCN production and CH_4 abundances, which was further quantified by Pearce et al. (2022a). HCN abundances for N_2 -dominated rocky planets vary considerably with C/O ratio, with Rimmer & Rugheimer (2019) finding low HCN production for $\text{C/O} \leq 0.5$, mixing ratios between 1–1000 ppm for $0.5 < \text{C/O} \leq 1.5$, and mixing ratios exceeding 0.1% for $\text{C/O} > 1.5$. The abundances also depend strongly on the UV irradiance, particularly short wavelengths: 50–100 nm and 100–200 nm photons drive HCN production (N_2 photolysis) and destruction (H_2O photolysis), respectively (Rimmer & Rugheimer, 2019). Lightning can be an additional source of feedstock molecules like HCN (e.g., Chameides & Walker, 1981; Barth et al., 2024). Lightning is advantageously a tropospheric phenomenon, providing a more straightforward source of feedstock molecules to aqueous surface environments where once again the UV environment dictates further complexity (e.g., Ranjan & Sasselov, 2016).

Considering modern Earth, we see considerable spatial and temporal variations in chemical abundances (e.g., ozone and methane distributions), caused by a combination of photochemistry, atmospheric circulation, and spatially varying emissions. For rocky exoplanets, diverse orbital configurations and host stars affect the climate (e.g., Joshi et al., 1997; Boutle et al., 2017; Del Genio et al., 2019; Turbet et al., 2022), atmospheric circulation (e.g., Haqq-Misra et al., 2018; Carone et al., 2018; Sergeev et al., 2022), and photochemically active regions (e.g., Proedrou & Hocke, 2016; Chen et al., 2018; Yates et al., 2020; Braam et al., 2025). Additionally, the effects of energetic processes such as stellar flares from M-dwarfs (Segura et al., 2010; Airapetian et al., 2016; Chen et al., 2021; Ridgway et al., 2023a) and lightning (Ardaseva et al., 2017; Braam et al., 2022; Barth et al., 2024) will affect the atmospheric chemistry with spatial and temporal variations. The complex interplay between all these processes is studied using 3D coupled climate-chemistry

models and, in turn, determines the appearance of spectroscopic observations of exoplanet atmospheres (e.g., Chen et al., 2021; Cooke et al., 2023; Braam et al., 2025). We can use the predicted environmental conditions of exoplanets to understand the atmospheric formation of feedstock molecules and determine the circumstellar abiogenesis zone, the zone in which life can originate for a given scenario (Rimmer et al., 2018; Rimmer, 2023). Claringbold et al. (2023) showed that many of these feedstock molecules have absorption signatures in mid-infrared wavelengths, likely below current detection limits but relevant for future missions specifically targeting terrestrial exoplanets, such as the Large Interferometer For Exoplanets (Quanz et al., 2022). Solar System detections of nitriles include HCN and HC₃N by Voyager in the IR on Titan (Hanel et al., 1981; Kunde et al., 1981), as well as HCN on Neptune (Rosenqvist et al., 1992; Marten et al., 1993), Jupiter (Marten et al., 1995), and Saturn (Benmahi et al., 2022).

To anticipate future exoplanet atmospheric observations and connect atmospheric synthesis of feedstock molecules to known exoplanet parameters (irradiation, orbit), photochemical models are applied. These models (1D or 3D) fundamentally depend on the chemical kinetics and the implemented chemical network (the set of photo- and thermochemical reactions). Therefore, our understanding of the underlying chemical processes and knowledge of reaction rate coefficients is crucial to these photochemical studies (Winiberg et al., 2025). Uncertainties in a single or multiple measurements of rate coefficients, as well as extrapolation outside the measured temperature and pressure ranges, affect predictions from a chemical network. Limitations on network sizes, including the lumping together of multi-step reactions into a single one, further influence network predictions. The scenario of interest is also relevant: chemical networks of Solar System atmospheres are topologically distinct, with unique features for Earth's network presenting a potential biosignature (Solé & Munteanu, 2004; Wong et al., 2023; Fisher et al., 2025). For oxidised environments like modern Earth, chemical networks were constructed decades ago and regularly improved (e.g., Chapman, 1930; Bates & Nicolet, 1950; Crutzen, 1970; Logan et al., 1981; Jacob, 2000; Archibald et al., 2020). Chemical networks were also developed to explain observed disequilibrium chemical abundances in Jupiter's atmosphere (e.g., Fegley & Lodders, 1994; Moses et al., 2005; Visscher et al., 2010) and for the high temperatures of hot Jupiters (e.g., Zahnle et al., 2009; Moses et al., 2011; Venot et al., 2012). The reducing environment of Early Earth has similarities to Titan, and thus chemical networks for the Early Earth (Zahnle, 1986; Pavlov et al., 2001; Pearce et al., 2020a) incorporate relevant reactions from chemical networks for Titan (Yung et al., 1984; Hébrard et al., 2007; Lavvas et al., 2008; Krasnopolsky, 2009; Loison et al., 2015; Dobrijevic et al., 2016; Willacy et al., 2016; Vuitton et al., 2019). Other networks were constructed to treat reducing to oxidising conditions (Rimmer & Helling, 2016; Tsai et al., 2021). Rimmer & Helling (2016) collect all the available rate coefficient data into a large network, which was benchmarked for several scenarios. The Consistent Reduced Atmospheric Hybrid Chemical Network with Oxygen extension (CRAHCN-O) was constructed to simulate the formation of simple feedstock molecules in planetary atmospheres and is a relatively small network of a few hundred reactions (Pearce et al., 2019, 2020a,b). Quantum chemical calculations were used to explore previously unknown reactions and determine rate coefficients, and the network was applied to the atmospheres of Titan and Early Earth (e.g., Pearce et al., 2020b, 2022b). Regardless of choices in network construction, the uncertainties in rate coefficients present an issue for chemical networks and their applications (Lira-Barria et al., 2024).

Specifically for the implementation in 3D atmosphere models, the computational cost rises rapidly with a larger number of species and/or reactions, making small networks like CRAHCN-O attractive. Several approaches for network reduction, which aim to simplify large chemical networks without compromising accuracy, have been applied in the context of exoplanets. These include a pathway analysis to inform the network reduction (Tsai et al., 2018, 2022; Lee et al., 2023), detailed kinetic analyses with commercial software (Venot et al., 2019), and a genetic algorithm to quantify network sensitivity and find optimal solutions for reduction (Lira-Barria et al., 2024). Pathway analyses find the shortest path to form species *b* from species *a*, which depend on the local pressure, temperature, and actinic flux (Tsai et al., 2018). Beyond network reductions, pathway analyses enable the comparison of different chemical networks when focusing on a particular species of interest.

In this paper, we present the implementation of the CRAHCN-O chemical network into the VULCAN photochemical kinetics code (Tsai et al., 2017, 2021). We test the atmospheric production of hydrocarbons and feedstock molecules for planets orbiting M stars and compare this to predictions from the standard N-C-H-O network in VULCAN. We present our simulation setup and describe both chemical networks in Section 2. In Section 3, we compare the abundances predicted by both networks, describe the role of photochemical shielding, and identify the key pathways and chemical mechanisms affecting feedstock molecules. In Section 4, we demonstrate the effect of the shielding mechanism, put our results into context, and conclude our study.

2. Methods

2.1. Modelling framework

VULCAN is an open-source 1D photochemical kinetics code that solves the mass continuity equations for the temporal evolution of the number density of chemical species (Tsai et al., 2017, 2021). The reactions in the chosen chemical network define the interactions between different species and are driven by the background temperature-pressure and vertical mixing profiles, a set of boundary conditions, and the incoming stellar radiation. In what follows, we describe the details of our simulation setup and changes to the chemical network and refer the reader to Tsai et al. (2017, 2021) for an extensive description of VULCAN.

In this study, we simulate the atmosphere of Proxima Centauri b (Anglada-Escudé et al., 2016), the nearest exoplanet to Earth at 1.3 pc, to benchmark production of hydrocarbons and feedstock molecules. Proxima Centauri b is expected to be tidally locked to its host star at an orbital distance of 0.0485 AU and with a period of 11.186 days (e.g., Goldreich & Peale, 1966; Barnes, 2017). Following Turbet et al. (2016), we use a radius of $1.1 R_{\oplus}$ and gravity of 10.90 m s^{-2} . For the stellar spectrum of Proxima Centauri (or GJ 551), we use version 2.2 from the MUSCLES spectral library¹ (France et al., 2016; Youngblood et al., 2016; Loyd et al., 2016) as shown in Figure 1a. Comparing the spectral radiant flux density $F(\lambda)$ received by Proxima Centauri b with that received by Earth, we see that the M5.5V spectrum peaks at higher wavelengths and that Proxima Centauri b receives substantially larger fluxes in the near-UV and far-UV wavelength regions (e.g., Ribas et al., 2017). We consider the quiescent stellar spectrum as the driver of photochemistry, but note that stellar activity enhances the stellar UV and X-ray fluxes (Vida et al., 2019), potentially affecting the space weather and atmospheric chemistry (Garraffo et al., 2016; Airapetian et al., 2020; Ridgway et al., 2023b) of the planet. We include additional simulations using the stellar spectra of GJ 436 (M2.5V) from the MUSCLES survey, as well as GJ 676 A (M0V) and TRAPPIST-1 (M8V) from the Mega-MUSCLES survey (Wilson et al., 2021, 2024), to explore the sensitivity of network differences to different spectral energy distributions. For each star, we simulate the photochemistry at the distance for which the irradiance equals that received by Proxima Centauri b, whilst keeping all the other parameters the same. The irradiance criterion results in semi-major axes of 0.35 AU (GJ 676 A), 0.18 AU (GJ 436), and 0.028 AU (TRAPPIST-1) and gives the spectral radiant flux densities in Figure 1a.

The temperature profile follows from simulations with a 3D coupled climate-chemistry model as presented in Braam et al. (2022), assuming a surface pressure of 1 bar. We calculate the mean dayside temperature – since this is the region with active photochemistry – and follow the temperature profile of Earth for pressures lower than 6×10^{-7} bar (see the solid red line in Figure 1b). For comparison, Figure 1b also shows the mean temperature profile of Earth's atmosphere. The troposphere is visible for $P > 0.1$ bar (the tropopause). Between $0.1 - 10^{-5}$ bar, we see the relatively stable stratosphere and mesosphere. For $P < 10^{-6}$ bar, we see the rising temperatures characteristic of the thermosphere. Except for the absence of a stratospheric inversion – due to varying strengths of radiative heating with stellar type (Godolt et al., 2015; Kozakis et al., 2022; De Luca et al., 2024) – the temperature profile is qualitatively similar to Earth. The eddy diffusion coefficient (K_{zz}) parametrises vertical mixing as a 1D diffusion process and is shown as the navy line in Figure 1b. Since no universal derivation of the K_{zz} profile currently exists (see e.g. Baeyens et al., 2021) and because of the similarities with the Earth's temperature profile, we opt for the Earth-like K_{zz} profile following Tsai et al. (2021) and Massie & Hunten (1981).

We consider N_2 -dominated atmospheres of 1 bar containing: 1) 400 ppm CO_2 , 2) 1% CO_2 based on Arney et al. (2017), and 3) 10% CO_2 following Rimmer & Rugheimer (2019), as shown in Table 1. For each CO_2 scenario, we vary the amount of CH_4 to probe the carbon-to-oxygen (C/O) ratio from 0.5 to 1.5, based on the reported sensitivity of HCN chemistry to C/O ratios within this range (Rimmer & Rugheimer, 2019). The initial mixing ratios are constant with pressure, except for H_2O , which is fixed at the surface to a mixing ratio of 0.00894 (corresponding to 25% relative humidity). Except for the fixed surface H_2O , all initial mixing ratios evolve chemically in the simulations. Given the H_2O and CO_2 profiles, the 400 ppm CO_2 case is the most radiatively consistent for the temperature profile in Figure 1. Note that we keep the temperature and K_{zz} profiles fixed to focus on changes in the chemistry. Because of the adjusted N_2 mixing ratios for the 1% and 10% CO_2 cases, the carbon-to-nitrogen (C/N) ratio also changes, as shown in Table 1. The variations in C/N ratio are most prominent for the 10% CO_2 case, since CO_2 and CH_4 account for up to 20% of the atmosphere. C/N variations are small for the 1% CO_2 and 400 ppm CO_2 case, as N_2 mixing ratios do not go below 96% and 99.9%, respectively. Hence, beyond comparing the effect of C/O ratios, the contrast between the three setups can show the effect of varying C/N ratios on the final chemical abundances. Since the initial abundance of CH_4 is varied with C/O ratio, we also change the H/O ratio. For the photochemistry around M stars other than Proxima Centauri, we

¹<https://archive.stsci.edu/prepds/muscles/>

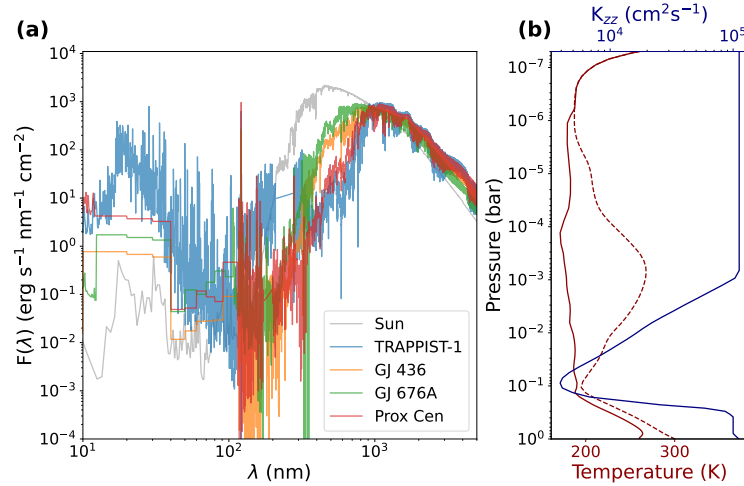


Figure 1: Background stellar and planetary environments: (a) the spectral radiant flux density as received by Proxima Centauri b and planets around different M-type stars receiving the same irradiance, compared to the Solar flux at 1 AU. Panel (b) shows vertical profiles of the temperature from Braam et al. (2022) (solid line) compared to Earth's temperature profile (dashed line) and eddy diffusion (K_{zz}), following Tsai et al. (2021) and Massie & Hunten (1981).

Table 1

Initial compositions for all CO₂ cases (400ppm, 1%, and 10% CO₂). The 400 ppm case is most radiatively consistent with Figure 1, 1% CO₂ case is based on Arney et al. (2017), and the 10% CO₂ case on Rimmer & Rugheimer (2019)

CO ₂ Level	C/O	C/N	H/O	N ₂	H ₂ O	O ₂	CO ₂	CH ₄
400ppm	0.5	2e-4	2e-4	0.999	1e-6	0.0	4e-4	0.0
	0.75	3e-4	1.001	0.999	1e-6	0.0	4e-4	2e-4
	1.0	4e-4	2.000	0.999	1e-6	0.0	4e-4	4e-4
	1.25	5e-4	2.999	0.999	1e-6	0.0	4e-4	6e-4
	1.5	6e-4	3.998	0.999	1e-6	0.0	4e-4	8e-4
1%	0.5	5.1e-3	1e-4	0.98	1e-6	1e-8	0.01	0.0
	0.75	7.7e-3	1.000	0.98	1e-6	1e-8	0.01	0.005
	1.0	1.03e-2	2.000	0.97	1e-6	1e-8	0.01	0.01
	1.25	1.29e-2	3.000	0.97	1e-6	1e-8	0.01	0.015
	1.5	1.56e-2	4.000	0.96	1e-6	1e-8	0.01	0.02
10%	0.5	5.62e-2	1e-5	0.89	1e-6	0.0	0.1	0.0
	0.75	8.93e-2	1.000	0.84	1e-6	0.0	0.1	0.05
	1.0	0.127	2.000	0.79	1e-6	0.0	0.1	0.1
	1.25	0.169	3.000	0.74	1e-6	0.0	0.1	0.15
	1.5	0.217	4.000	0.69	1e-6	0.0	0.1	0.2

use the same setups but only consider C/O ratios of 0.5, 1.0, and 1.5. The runs exclude surface emissions or deposition of chemical species, to focus on differences caused by employing distinct chemical networks.

2.2. Chemical Networks

2.2.1. VULCAN N-C-H-O

The first version of VULCAN included the C-H-O network (Tsai et al., 2017), which Tsai et al. (2021) extended to also include nitrogen and sulfur chemistry. Here, we use the full version of the N-C-H-O network, covering reducing to oxidising conditions and including network updates from Tsai et al. (2024). This version of N-C-H-O contains a total of 417 (gas-phase) chemical reactions that connect 73 species, including 349 bimolecular and 68 termolecular reactions. Additionally, 57 photodissociation reactions are considered. All the thermochemical reactions are reversed using an equilibrium constant (Heng et al., 2016; Tsai et al., 2017). Generally, reaction rate coefficients are taken from

the NIST database², the KIDA database³, and literature sources including Moses et al. (2005); Lavvas et al. (2008); Moses et al. (2011), and Zahnle et al. (2016). Many thermochemical reactions are valid for a wide temperature range (300–2500 K), although the experimental data for some are limited to narrow temperature ranges. The condensation of H₂O is also included. The N-C-H-O network has been evaluated for hot Jupiters HD 189733 b and HD 209458 b (using other photochemical models) and for measured abundances in the atmospheres of Jupiter and present-day Earth.

Hydrocarbons are generally truncated at 2 carbon atoms due to limitations of the kinetics data (Venot et al., 2015), except for select higher-order species up to C₆ that act as sinks for C₂ hydrocarbons and potential haze precursors, particularly benzene (Tsai et al., 2021). The top panel of Figure 2 shows the species in N-C-H-O as nodes and the reactions between them as edges. Atomic hydrogen is clearly central to this network and involved in the most reactions (86). HCN is involved in 39 reactions. H₂CO is less central to the chemical processes in the network, with a total of 31 reactions. We see the inclusion of some higher-order hydrocarbons – those with three or more carbon atoms – such as allene (C₃H₄ or CH₂CCH₂), diacetylene (C₄H₂), 1-butene-3-yne-1-yl radical (C₄H₃), benzene (C₆H₆). However, the peripheral location and limited number of reaction connections (up to 8) of most of these higher-order hydrocarbons indicate their role as sinks for the C₂ species. Several hydrocarbons with fewer than three carbon atoms are more central to the chemical network and participate in a significantly larger number of reactions: examples are CH₄ with 43 reactions, methyl radical (CH₃) with 79, methylene (CH₂) with 46, methyldiyne radical (CH) with 36, acetylene (C₂H₂) with 49, and ethane (C₂H₆) with 15.

2.2.2. CRAHCN-O

The CRAHCN-O network⁴ is a relatively small chemical network developed to model the production of feedstock molecules in planetary atmospheres (Pearce et al., 2019, 2020a,b). The coupling between computational quantum chemistry with canonical variational transition state theory and Rice-Ramsperger-Kassel-Marcus/master equation theory allows the exploration of previously unknown reactions and the consistent calculation of reaction rate coefficients for thermochemical reactions (Pearce et al., 2019, 2020a,b). The resulting reactions are collected in the CRAHCN-O network that focuses on the accurate simulation of HCN and H₂CO production in CO₂-, N₂-, H₂O-, CH₄-, and H₂-dominated atmospheres and are valid for temperatures of 50–400 K. CRAHCN-O contains experimental data where available and is supplemented by the consistently calculated quantum chemical rate coefficients where experimental data is missing (Pearce et al., 2020a). Updates to the CRAHCN-O were presented in later work by Pearce et al. (2022b) and Pearce et al. (2022a). The CRAHCN-O network has been used to model HCN on Titan (Pearce et al., 2020b) and HCN and H₂CO on the early Earth (Pearce et al., 2022a,b).

Here, we use the publicly available version 3 of CRAHCN-O⁴ that includes further updates. In total, the network contains 399 forward gas-phase reactions, consisting of 336 bimolecular and 63 termolecular reactions. All of these are reversed in VULCAN. Figure 2 shows that OH (involved in 72 reactions) and H (62 reactions) are the most important in the CRAHCN-O network. CRAHCN-O has more reactions involving HCN (59) and H₂CO (41), both of which also have a central position in the network. Because of its focus on simple feedstock molecules, CRAHCN-O simulates hydrocarbons only up to two carbon atoms, resulting in fewer reaction connections for species like CH₄ (31), CH₃ (48), CH₂ (37), and C₂H₂ (26), as compared to N-C-H-O. CH (40) and C₂H₆ (13) are exceptions with a higher and similar number of reactions, respectively.

2.2.3. Implementing CRAHCN-O into VULCAN

The rate coefficients in CRAHCN-O follow the Arrhenius law at a reference temperature of 300 K:

$$k = A' \left(\frac{T}{300} \right)^b \exp \left(-\frac{E'_a}{T} \right). \quad (1)$$

Since VULCAN uses the Arrhenius law at a reference temperature of 1 K, we need to incorporate the reference temperature into $A = A'/300^b$, which was done for both the bimolecular and termolecular reactions. A total of 49 bimolecular reactions that were initially added in Pearce et al. (2022a) are presented inconsistently for a reference temperature of 1 K and with E'_a in cal mol⁻¹, whereas E_a in VULCAN is already normalised by the gas constant and thus has units K. For these 49 reactions, we normalise E'_a from CRAHCN-O by the specific gas constant in the

²<https://kinetics.nist.gov/kinetics/>

³<https://kida.astrochem-tools.org/>

⁴<https://github.com/bennski/CRAHCN>

Table 2

Duplicate reactions in CRAHCN-O and, where available, their coefficients as given in N-C-H-O. Mostly, these reactions are represented by a set of rate coefficients for the forward (first column) and reverse reaction (second column). Occasionally, the reaction is simply duplicated, with the same coefficients in both columns. The H_2CN coefficients are specified for two distinct temperature ranges. The reaction used for the VULCAN adaptation is highlighted in bold. References are indicated by numbers in the last column and listed as footnotes below the table.

Reaction	[A (cm ³ s ⁻¹ or cm ⁶ s ⁻¹), b, E _a (K)]		N-C-H-O	(k ₃₉₈) (cm ³ s ⁻¹ or cm ⁶ s ⁻¹)			Ref
	CRAHCN-O	CRAHCN-O 2		CRAHCN-O	CRA. 2	N-C-H-O	
O + H ₂ CN → HCNO + H	[3.13e-17, 1.72, 788]	[9.8e-11, 0, 0]	[N/A]	4.01e-14	9.8e-11	N/A	1
HCN + O → NCO + H	[5.44e-14, 0.96, 4039.8]	[4.15e-11, 0.2, 5743.2]	[4.5e-15, 1.58, 13400]	1.67e-17	5.53e-19	1.08e-30	2
H ₂ O + CH → OH + CH ₂	[6.64e-14, 0.38, 2178]	[7.6e-13, 0, 0]	[1.43e-18, 2.02, 3410] [†]	3.87e-16	7.6e-13	1.53e-18	3
O + CH ₄ → CH ₃ + OH	[1.5e-15, 1.56, 4269.8]	[4.97e-12, -0.29, 4139]	[1.16E-19, 2.2, 2240] [†]	6.5e-18	8.85e-19	1.75e-17	4
O + H ₂ → OH + H	[8.51e-20, 2.67, 3163.2]	[8.11e-21, 2.8, 1950.0]	[8.52E-20, 2.67, 3160]	8.44e-18	9.88e-17	8.54e-18	5
O(¹ D) + H ₂ CN → HCNO + H*	[2.13e-10, -0.39, 1070]	[1.41e-26, 5.3, -356]	[N/A]	6.37e-13	6.04e-13	N/A	6
O(¹ D) + H ₂ CN → OH + HCN*	[1.52e-9, -0.81, 1386]	[5.57e-25, 4.56, -46]	[N/A]	1.44e-13	1.25e-13	N/A	7
HCN + H → HNC + H	[9.59e-14, 1.2, 6249]	[9.28e-13, 0.8, 649]	[N/A]	6.98e-20	1.00e-11	N/A	8
CH ₄ + CH ₂ → CH ₃ + CH ₃	[1.9e-31, 7.45, 3401]	[5.3e-11, 0, 0]	[4.09e-18, 2, 4162]	5.69e-18	5.3e-11	3.12e-19	9
H + CH ₄ → CH ₃ + H ₂	[2.19e-20, 3, 4045]	[1.14e-20, 2.74, 4740]	[2.2e-20, 3, 4040]	7.38e-19	8.48e-21	7.54e-19	10
CH ₂ + H ₂ → H + CH ₃	[3.28e-36, 9.04, 1450]	[3.68e-14, 1.15, 6529]	[7.32E-19, 2, 3699]	5.88e-16	7.87e-21	2.64e-19	11
H + CH ₂ → CH + H ₂	[2e-10, 0, 0]	[3.1e-10, 0, 1650]	[1.1e-11, 0, -900]	2e-10	1.22e-12	2.25e-10	12
NH ₂ + OH → NH ₃ + O	[1.83e-21, 2.6, 869.6]	[1.6e-11, 0, 3669]	[1.6e-11, 0, 3669] [†]	2.68e-16	7.2e-17	7.20e-17	13
CH ₃ OH + N → CH ₃ + HNO	[3.99e-10, 0, 4330]	[4e-10, 0, 4330]	[N/A]	1.95e-16	1.95e-16	N/A	14
CH ₃ OH + OH → H ₂ CO + H ₂ O + H	[3.01e-16, 1.44, 56]	[2.98e-16, 1.44, 56]	[N/A]	1.2e-13	9.03e-13	N/A	15
HO ₂ + NO → OH + NO ₂	[1.2e-13, 0, 0]	[3.01e-11, 0, 3361]	[3.6e-12, 0, -270]	9.12e-13	3.81e-16	8.91e-12	16
NO ₂ + N → N ₂ O + O	[5.8e-12, 0, -220]	[5.8e-12, 0, -220]	[5.8e-12, 0, -220]	1.21e-11	1.21e-11	1.21e-11	17
NO ₃ + CH ₃ O → H ₂ CO + HNO ₃	[1.5e-12, 0, 0]	[1.5e-12, 0, 0]	[N/A]	1.5e-12	1.5e-12	N/A	18
NO ₂ + CH ₃ O → H ₂ CO + HNO ₂	[3e-13, 0, 0]	[3e-13, 0, 0]	[N/A]	3e-13	3e-13	N/A	19
CH ₃ + OH → CH ₂ OH + H	[1.2e-12, 0, 2760]	[1.6e-10, 0, 0] [†]	[1.6e-10, 0, 0] [†]	1.14e-16	1.6e-10	1.6e-10	20
CH ₃ O + CH ₃ OH → CH ₂ OH + CH ₃ OH	[5e-13, 0, 2050]	[5e-13, 0, 2050]	[N/A]	5.14e-16	5.14e-16	N/A	21

[1]Pearce et al. 2020a [2]Pearce et al. 2020a [3]Pearce et al. 2020a [4]Baulch et al. 1992 [5]Baulch et al. 1992 [6]Pearce et al. 2020a [7]Pearce et al. 2020a [8]Pearce et al. 2019 [9]Pearce et al. 2019 [10]Baulch et al. 1992 [11]Pearce et al. 2019 [12]Pearce et al. 2020a [13]Baulch et al. 1992 [14]Roscoe & Roscoe 1973 [15]Srinivasan et al. 2007 [16]Tsang & Herron 1991 [17]Demore et al. 1997 [18]Kukui et al. 1995 [19]Atkinson et al. 1989 [20]Tsang 1987 [21]Tsang 1987

* The two sets of rate coefficients represent two temperature ranges, 50–200 K and 200–400 K, respectively.

[†] The coefficients in the N-C-H-O network represent the reverse reaction.

data required for reversing the rates (see Appendix E of Tsai et al., 2017). For the sake of network comparison, we consider the same photodissociation reactions in both networks where possible. Since several species that are included in the N-C-H-O network are not present in CRAHCN-O, this results in the removal of the photolysis of HNCO, N₂H₄ (2 branches), N₂O₅ (2 branches), C₆H₆ (2 branches), and C₄H₂ for the CRAHCN-O implementation.

VULCAN calculates the reverse reaction rates from the forward rate coefficients and equilibrium constant (Tsai et al., 2017). In CRAHCN-O, several reverse reactions have specified rate coefficients, as listed in Table 2. For these duplicate reactions, we compared the rate coefficients with those in the NIST Chemical Kinetics Database⁵, and chose the coefficients from the most recent review that were measured in the relevant temperature range (180–400 K). The chosen coefficients are shown in bold and their respective references are also listed in Table 2. Initial testing of the CRAHCN-O network with standard VULCAN settings for convergence parameters revealed numerical instabilities in the chemical solver when using the CRAHCN-O network. This was especially observed for the 100 ppm CO₂ cases, suggesting an important role for trace gases in the chemical evolution in CRAHCN-O. Therefore, we reduced the absolute tolerance to 10⁻⁸, slowing down the runs but increasing their accuracy. Previous simulations with the ChemKM photochemical kinetics model and CRAHCN-O use an absolute tolerance of 10⁻⁹⁹ (Pearce et al., 2022b). The relative tolerance is set to 0.05, in line with typical values (Tsai et al., 2017).

2.3. Pathway Analysis

The conversion of one chemical species to another usually involves a multi-step reaction with intermediate species, together forming a pathway or cycle between them. Examples of such pathways on Earth are the Chapman mechanism forming ozone from molecular oxygen (Chapman, 1930) or the catalytic cycles destroying ozone back into oxygen (Bates & Nicolet, 1950; Crutzen, 1970). Other Solar System examples include the production of hydrocarbons on Titan (Yung et al., 1984; Lavvas et al., 2008; Krasnopolsky, 2009; Hébrard et al., 2013; Dobrijevic et al., 2016; Vuitton et al., 2019), seasonal CH₄ variations on Mars potentially explained by heterogeneous HCl chemistry (Taysum et al., 2024), and the CO–CH₄ conversion on Jupiter (Prinn & Barshay, 1977; Visscher et al., 2010). Chemical cycles are also important for the CO–CH₄ conversion on brown dwarfs (Zahnle & Marley, 2014) or hot Jupiters (Moses et al., 2011) and can explain the observed SO₂ abundances for WASP-39b (Tsai et al., 2023).

Here, we follow Tsai et al. (2018) and perform a pathway analysis based on Dijkstra's algorithm (Dijkstra, 1959) to find the fastest paths in graph theory. In considering a chemical network as a graph, the chemical species represent

⁵Standard Reference Database 17, Version 7.1 (Web Version), Release 1.6.8: <https://kinetics.nist.gov/kinetics/>

nodes and reactions represent edges connecting the nodes, as depicted in Figure 2. A faster reaction implies a shorter edge, proportional to $1/r_j$, where r_j is the rate of reaction j in molecules $\text{cm}^{-3}\text{s}^{-1}$. Based on the summed inverse rates between node A to node B (considering all intermediate nodes), Dijkstra's algorithm then finds the shortest paths between nodes A and B in the network. The chemical timescales for different intermediate steps in the pathways can differ by orders of magnitude, with the slowest reaction rate representing the bottleneck and thus the rate-limiting step (Moses et al., 2011) of a pathway. The simulated reaction rates depend on rate coefficients, temperature, pressure, actinic flux, and chemical abundances, which are reflected in the pathways and their rate-limiting steps (Tsai et al., 2022). A similar pathway analysis tool has been used to reduce the VULCAN N-C-H-O network for hot Jupiters to the rate-limiting steps of pathways as net reactions for an application in 3D climate-chemistry models (Tsai et al., 2022; Lee et al., 2023) and allowed to quantify photochemical pathways to SO_2 in the atmosphere of WASP-39 b (Tsai et al., 2023). Our study mainly focuses on pathways to produce feedstock molecules: from N_2 , CH_4 , and CO_2 to HCN and HC_3N , from CH_4 and CO_2 to H_2CO , and from CH_4 to hydrocarbons including C_2H_2 , C_2H_6 , C_3H_4 , and C_4H_3 .

3. Results

We start this Section by qualitatively analysing the vertical distributions of chemical species in each of the simulations and demonstrating the effects of photochemical shielding. We then present the abundances of species as a function of C/O ratio and show that the main network differences hold for other M-star types. Lastly, we compare reaction pathways to important feedstock molecules and present the chemical mechanisms that explain the hydrocarbon distributions for both networks.

3.1. Vertical Distributions

Following the initialisation with N_2 , H_2O , O_2 , CO_2 , and CH_4 , we show the steady state abundance profiles from the simulations in Figure 3, for different C/O ratios (rows) and the background scenarios of 400 ppm, 1 %, and 10 % CO_2 (columns). To compare the predictions from the CRAHCN-O network (solid) and N-C-H-O network (dashed) we selected initialisation species, feedstock molecules, and hydrocarbons based on the network comparison in Section 2.2.

For $\text{C/O}=0.5$, CO_2 is the main C-bearing species since CH_4 is initialised at zero abundance (see Table 1). The profiles of the most abundant species (CO_2 in brown and H_2O in grey) show good agreement between both chemical networks across the three CO_2 backgrounds. From the HCN profiles (blue), we see that the N-C-H-O network forms HCN for a range of pressures in the absence of CH_4 . For CRAHCN-O, the upper atmosphere ($>10^{-5}$ bar) shows HCN production. We further explore this inter-network difference in Section 3.3.1. Especially for the 400 ppm CO_2 cases, CO_2 abundances in the upper atmosphere are higher for CRAHCN-O. This is related to strong HCO formation, which allows regeneration of CO_2 .

When CH_4 becomes significant at $\text{C/O}>0.5$, the vertical profiles of most species begin to diverge between the two chemical networks. The maximum pressure of the CO_2 profile diverging scales with the initial CO_2 and CH_4 abundances. In the 400 ppm CO_2 scenario, CO_2 abundances are similar for $P>10^{-4}$ bar. For lower pressures with N-C-H-O, CO_2 photodissociation causes decreasing abundances. Higher abundances of CO_2 persist for $P<10^{-4}$ bar when using the CRAHCN-O network. In the 1% and 10% CO_2 scenarios, CO_2 vertical profiles are similar for $P>10^{-5}$ and $P>10^{-6}$ bar, respectively. For lower pressures, we again simulate fast photochemical destruction with the N-C-H-O network and significantly higher abundances with CRAHCN-O. Evidently, photochemical processes must be responsible for the divergence in CO_2 profiles. With the higher initial CO_2 (and CH_4) when moving from left to right columns in the plot, the enhanced attenuation of stellar radiation keeps the photochemical impact limited to smaller portions of the low-pressure upper atmosphere regions. The difference seems to indicate that a strong UV-absorbing species (at similar wavelengths to CO_2) forms in substantial abundances for CRAHCN-O when CH_4 is present at $\text{C/O}>0.5$, shielding CO_2 from photodissociation.

The inter-network differences in CH_4 (pink) profiles also depend on atmospheric pressure, with profiles that are similar for relatively high pressures and diverge strongly in the photochemically dominated low-pressure regions. For N-C-H-O, the photochemical destruction of CH_4 extends to higher pressures than that of CO_2 . Again, the increased CH_4 abundance from left to right columns moves the photochemical regions upwards to lower pressure. However, the inter-network differences show that CH_4 abundances persist to much lower pressures for CRAHCN-O. Evidently, the UV-absorbing species that forms considerably from CH_4 with CRAHCN-O in turn shields CH_4 from the photochemical destruction seen with N-C-H-O. At first glance, H_2O profiles seem to show similar behaviour as CH_4 . In both networks,

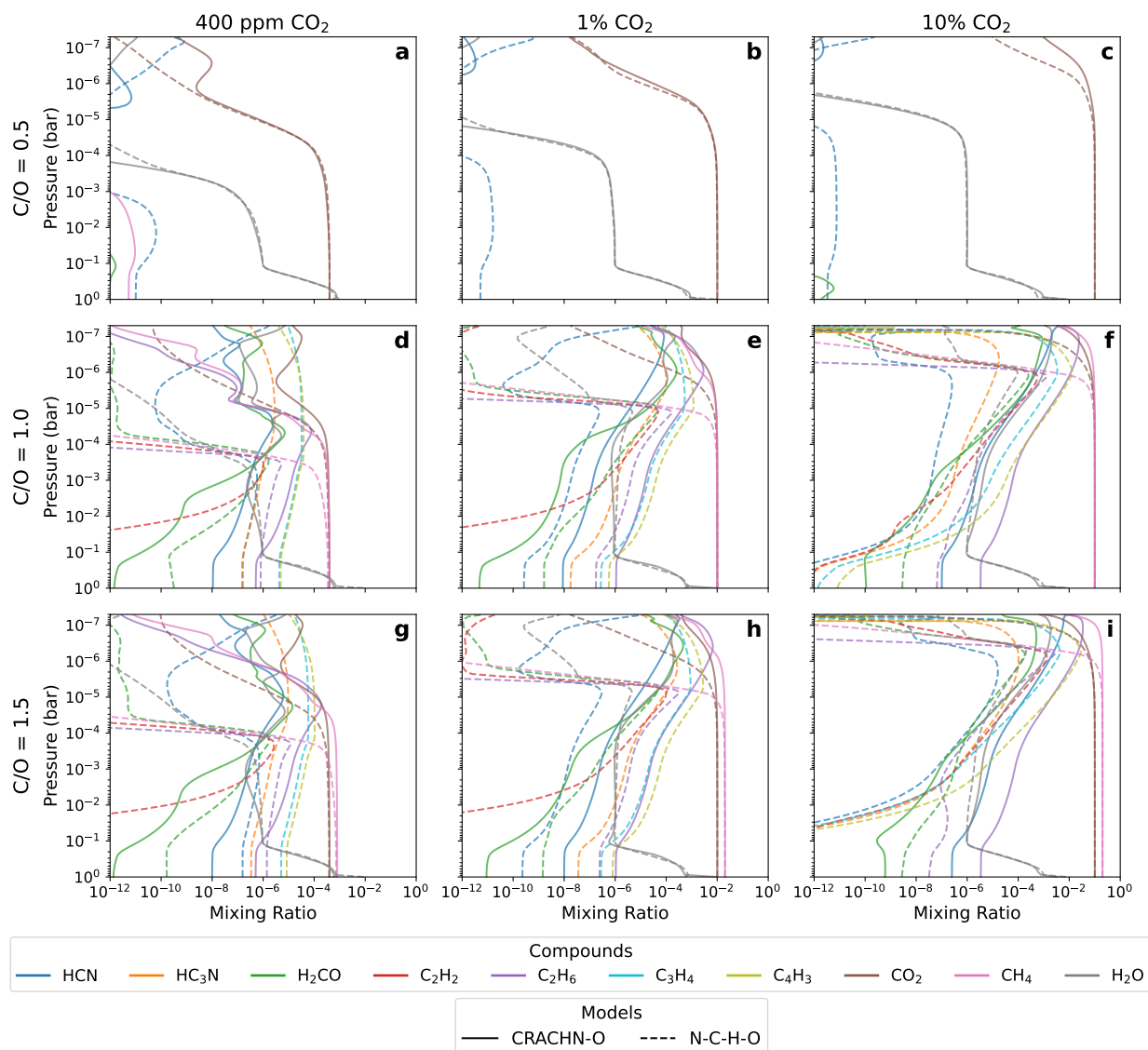


Figure 3: Grid of selected mixing ratios versus atmospheric pressure for VULCAN/CRAHCN-O and VULCAN/N-C-H-O simulations. The horizontal rows correspond to $C/O=0.5$ (a-c), 1.0 (d-f), and 1.5 (g-i), respectively. Each column shows one of the background CO_2 cases: 400 ppm (left), 1% (middle), and 10% (right). Solid lines correspond to the VULCAN/CRAHCN-O and dashed lines to the VULCAN/N-C-H-O simulations. The selected chemical compounds are part of the initialisation (CO_2 , CH_4 , H_2O) and prebiotically relevant (HCN , H_2CO , C_2H_2 , C_2H_6 , C_4H_3).

the photochemical destruction of H_2O moves to lower pressures with increasing CH_4 abundances. Nevertheless, inter-network differences in H_2O are not just due to photochemical shielding: further investigation shows that CRAHCN-O has net production of H_2O in the upper atmosphere through the reaction $OH + CH_2 \longrightarrow H_2O + CH$, which increases with increasing CH_4 abundance. Additional tests (not shown) with the other rate coefficients for this reaction in Table 2 resulted in decreased H_2O abundances but negligible effects for other compounds in Figure 3 since CO_2 is the main O-bearing species in all cases.

The differences in CH_4 and CO_2 profiles, as well as the shielding species, affect the profiles of feedstock molecules such as HCN , HC_3N (orange), and H_2CO (green). First, the production of these feedstock molecules will depend on where the photochemistry of CH_4 , N_2 , and CO_2 take place. Second, as illustrated by the accumulation of HCN and H_2CO at low pressures ($P < 10^{-4}$ for the 400 ppm case, $< 10^{-5}$ for the 1% case, $< 10^{-6}$ bar for the 10% case)

with CRAHCN-O, photochemically driven destruction processes of the feedstock molecules also weaken due to the attenuation of stellar radiation by photochemical shielding. Importantly for HCN, O and NO are much more abundant at low pressures for N-C-H-O, indicating that oxidising species from H₂O and CO₂ photolysis drive the destruction of HCN (see e.g., Rimmer & Rugheimer, 2019). For the 10% CO₂ case specifically, HCN abundances disappear for $P > 10^{-2}$ bar. For N-C-H-O at higher pressures ($P < 10^{-4}$ for the 400 ppm case, $< 10^{-5}$ for the 1% case, $< 10^{-6}$ bar for the 10% case), we see higher HCN mixing ratios than those in CRAHCN-O for 400 ppm CO₂ but lower mixing ratios for 1% and 10% CO₂. Notably different are the HC₃N profiles: it forms considerably in N-C-H-O, including at low pressures, but only reaches mixing ratios up to 10^{-13} in CRAHCN-O. In Section 3.3.1, we investigate the causes of the distinct vertical profiles of nitriles.

The profiles of C₂H₂ (red) reveal stark inter-network differences. Generally, the N-C-H-O network produces significantly more C₂H₂ than CRAHCN-O, with the peak in the abundances at $P \sim 10^{-4}$ for the 400 ppm CO₂ case, $\sim 10^{-5}$ for 1% CO₂, and $\sim 10^{-6}$ bar for 10% CO₂. The pressure levels agree with the onset of photochemical CH₄ destruction. For the CRAHCN-O network, either C₂H₂ production pathways are very slow or C₂H₂ destruction pathways are much faster compared to N-C-H-O. A detailed analysis of these pathways will follow in Section 3.3.3. C₂H₆ (purple) consistently forms more abundantly in the CRAHCN-O network, with abundances that are 1–2 orders of magnitude higher for $P > 10^{-4}$ bar (400 ppm CO₂ scenario), $P > 10^{-5}$ bar (1% CO₂ scenario), and $P > 10^{-6}$ bar (10% CO₂ scenario). The C₂H₆ abundances increase even further for lower pressures in the CRAHCN-O network, exceeding mixing ratios of 1% in the 10% CO₂ scenario, contrary to the strong decrease in the N-C-H-O network. Seemingly, differences in either C₂H₆ production or destruction allow for the upper atmospheric buildup with CRAHCN-O and strong depletion with N-C-H-O. A possible explanation is that CRAHCN-O simulates hydrocarbons only up to C₂H₆ (see Figure 2), allowing for its accumulation. N-C-H-O includes higher-order hydrocarbons such as C₃H₃, C₃H₄, C₄H₂, C₄H₃, C₄H₅, or C₆H₆, albeit with limited coverage of their potential interactions (see Figure 2). C₄H₃ (yellow line in Figure 3) and C₃H₄ (cyan) are the most abundant hydrocarbons with N-C-H-O. C₄H₃ and C₃H₄ abundance profiles follow a similar shape, with mixing ratios up to one order of magnitude higher for the former.

The C₂H₆ abundance in the upper atmosphere is crucial, due to its known UV shielding effects (e.g., Yoshida et al., 2024), potentially affecting the distributions of all the other species in Figure 3. We further investigate the photochemical shielding by plotting the UV photosphere in Figure 4. The black lines indicate the pressure levels at which the atmosphere becomes optically thick to stellar radiation at these wavelengths, and coloured lines denote the individual contributions of important absorbing species. First focusing on the top row, we see that photons with $\lambda < 115$ nm are predominantly absorbed by N₂, CO, and CO₂. For the N-C-H-O network at 400 ppm (Figure 4a), the same species dominate the absorption of photons with $\lambda > 115$ nm until scattering takes over for $\lambda > 180$ nm (not shown). However, some narrow wavelength regions are visible around 122 and 126 nm where CH₄ absorption dominates. Photons of these wavelengths can penetrate the atmosphere to $\sim 5 \times 10^{-4}$ bar before being absorbed. We see that this agrees with the onset of the strong decrease in CH₄ abundances with decreasing pressure, from the CH₄ profiles (dashed pink) in Figures 3d and g. For CRAHCN-O in Figure 4b, N₂, CO, and CO₂ similarly dominate the photon absorption at most wavelengths. However, an important difference with N-C-H-O is the shift of C₂H₆ absorption (violet) to lower pressure levels. C₂H₆ and CH₄ absorb photons at similar wavelengths, and the enhanced abundance with CRAHCN-O drives C₂H₆ absorption to lower pressures than CH₄, indeed shielding CH₄ from photodissociation. The same shielding applies to photolysis of CO₂, decreasing the abundances of O(³P) and NO and thus reducing the oxidising capacity of the atmosphere at low pressures. Moreover, C₂H₆ absorption dominates the UV photosphere in a few narrow wavelength regions between 115–145 nm and shifts the UV photosphere to lower pressures. Again in Figure 3d and g, the shielding by C₂H₆ explains why the onset of photodissociation starts at a lower pressure of $\sim 5 \times 10^{-5}$ bar.

For the 1% (Figure 4c–d) and 10% CO₂ (Figure 4e–f) cases, N₂, CO, and CO₂ again dominate for a broad range of wavelengths, but the inter-network differences between 115–145 nm are evident. With N-C-H-O, CH₄ dominates photon absorption between 115–132 nm to $\sim 10^{-5}$ bar (1% CO₂, Figure 4c) and $\sim 10^{-6}$ bar (10% CO₂, Figure 4e). Once again, these pressures agree with the pressure level at which the CH₄ starts to decrease dramatically with decreasing pressure (Figure 3). For CRAHCN-O, the photosphere is at a relatively low $P \sim 5 \times 10^{-6}$ bar (1% CO₂, Figure 4d) and $\sim 2 \times 10^{-7}$ bar (10% CO₂, Figure 4f). At the same time, C₂H₆ absorption dominates photon absorption at lower pressures than CH₄, again shielding the latter from photodissociation and thus supporting higher CH₄ (as well as CO₂) abundances down to the pressure levels of the UV photosphere. In turn, the shielding of CH₄ and CO₂ affects the photochemical balance of feedstock molecules, whilst C₂H₆ (and the enhanced CH₄ and CO₂) also directly shields feedstock molecules from photochemical destruction.

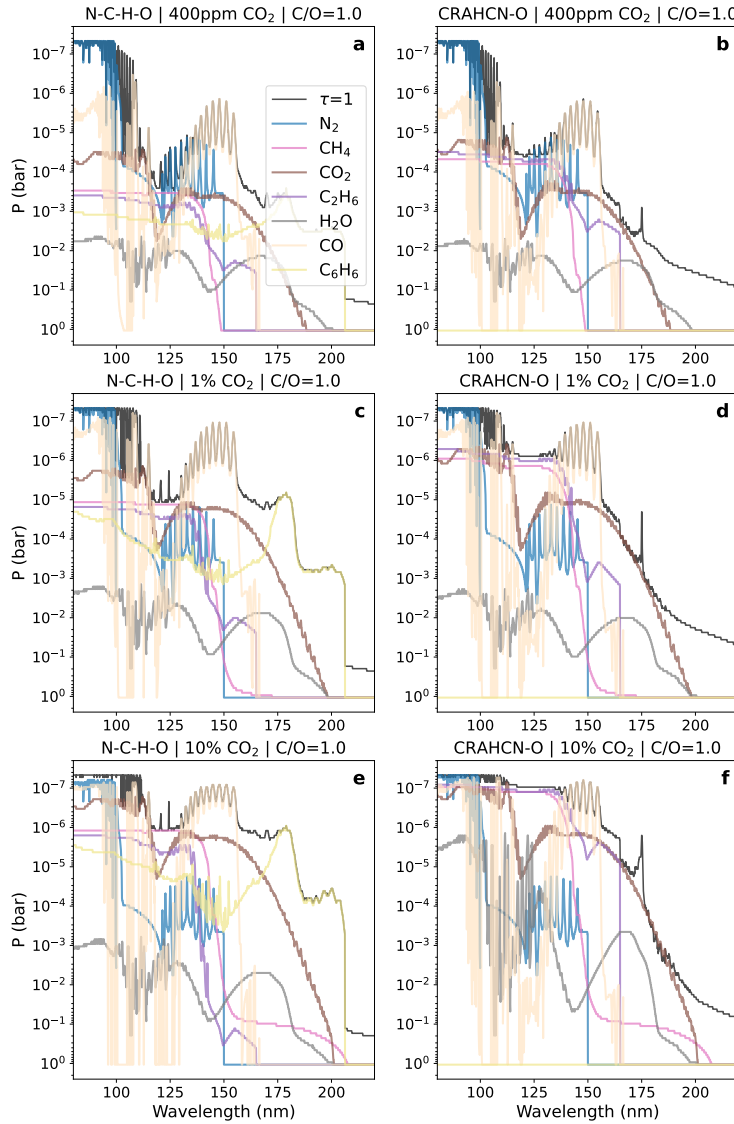


Figure 4: The UV photosphere, indicating the pressure level at which the atmosphere gets optically thick (optical depth $\tau = 1$) to incoming radiation, along with the individual contributions by important absorbing species for these wavelength ranges and background composition. Shown are the simulations with the N-C-H-O (a, c, e) and CRAHCN-O (b, d, f) network for the three CO_2 scenarios at $\text{C}/\text{O}=1.0$.

In Appendix A, we present an additional comparison to simulations with ARGO (Rimmer & Helling, 2016; Rimmer et al., 2021). ARGO solves the photochemistry-transport equation using a Lagrangian framework and includes the extensive STAND2020 chemical network of over 6000 reactions for 480 species, including ion-neutral chemistry. By comparing results for the 1% and 10% CO_2 scenarios, we find that the inclusion of ion chemistry in ARGO affects the photochemically active regions. Consequently, ARGO has strong CO_2 photochemical destruction down to higher pressures, and the effectiveness of photochemical shielding by hydrocarbons for $\text{C}/\text{O}>0.5$ lies in between that of N-C-H-O and CRAHCN-O. Using ARGO, peak HCN abundances agree best with CRAHCN-O, HC_3N with N-C-H-O, and H_2CO abundances are lowest out of all models. Hydrocarbons accumulate near the top of the atmosphere as C_3H_4 , which is not treated as photochemically active. These results further emphasise the need for enhanced understanding of hydrocarbon chemistry and the associated kinetic data in these scenarios.

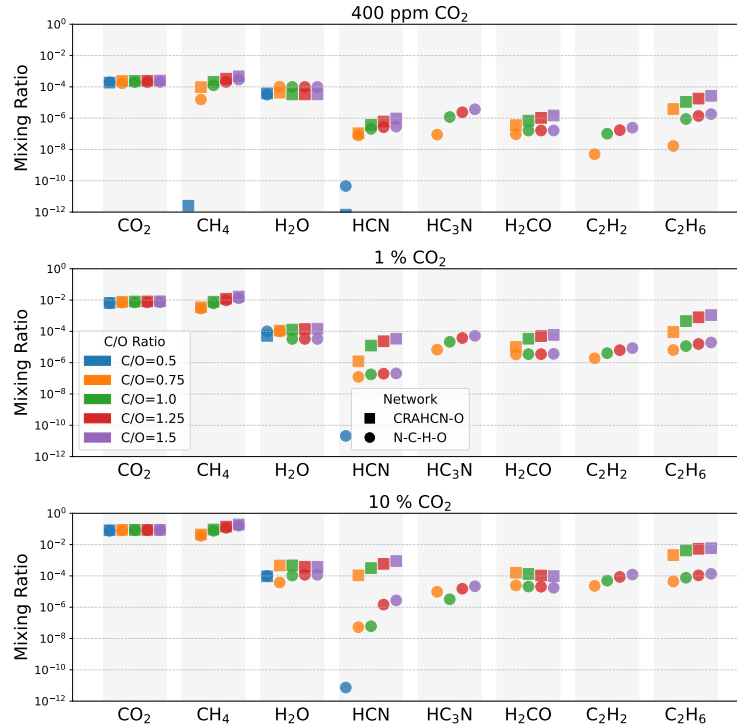


Figure 5: Vertically averaged mixing ratios from simulations with CRAHCN-O (squares) and N-C-H-O (circles), for 400 ppm CO₂ (top), 1% CO₂ (middle), and 10% CO₂ (bottom). For each species, the mixing ratios are shown as a function of C/O ratio as specified in Table 1.

3.2. Trends with C/O Ratio

We can infer the evolution of mixing ratios with C/O ratio for the individual networks from the vertically averaged mixing ratios in Figure 5, where each panel shows one of the background CO₂ scenarios. The vertical averages are not pressure-weighted, to focus on the shielding effects in the upper atmospheric regions. We briefly discuss the main outcomes. Except for the effects of photochemical shielding, the vertically averaged CO₂ mixing ratios remain comparatively constant, whereas CH₄ increases as a function of C/O. Figure 5 shows that these trends persist regardless of network and CO₂ scenario. Hydrocarbons (C₂H₂ and C₂H₆) generally increase with C/O, although at rather low mixing ratios (<10⁻¹⁶) for C₂H₂ in CRAHCN-O. The increased availability of CH₄ provides more material to form HCN and HC₃N, explaining the increasing abundance with C/O ratio in Figure 5 (note that HC₃N mixing ratios stay below <10⁻¹² for CRAHCN-O). In the 10% CO₂ case with the CRAHCN-O network, H₂O already peaks at the top of the atmosphere for C/O=1.0 (see Figure 3f), thus preventing a further increase in H₂O abundances with C/O ratio (bottom panel of Figure 5). H₂CO increases with C/O for the 400 ppm and 1% CO₂ scenarios, but decreases for 10% CO₂. This seems to indicate that its formation is CH₄-limited at lower abundances, but becomes O-limited with the decreased photodissociation of CO₂ and H₂O in the 10% CO₂ scenario. In Section 3.3.2, we explore the existence of pathways from both CO₂ and CH₄.

Given these general trends, we can investigate how inter-network differences evolve with the C/O ratio. Figure 6 compares the vertically averaged mixing ratios of the same set of species by calculating the ratio between CRAHCN-O and N-C-H-O predictions. Each panel indicates one of the background CO₂ scenarios. The first observation is that, for C/O>0.5, CRAHCN-O produces enhanced mixing ratios of CO₂, CH₄, HCN, H₂CO, and C₂H₆, regardless of the scenario. This can be traced back to the accumulation of C₂H₆ and its resulting photochemical shielding. Second, the trends of inter-network differences of CO₂, CH₄, and C₂H₆ as a function of C/O agree: a maximum enhancement with CRAHCN-O at C/O=0.75 for 400 ppm CO₂, increasing enhancements as a function of C/O for 1% CO₂, and decreasing enhancements as a function of C/O for 10% CO₂. Third, and also for C/O>0.5, HC₃N and C₂H₂ are much more abundant in N-C-H-O and stay below mixing ratios of 10⁻¹² for CRAHCN-O. Fourth, for C/O=0.5, the relative enhancement in N-C-H-O of HCN, HC₃N, H₂CO, and C₂H₂ (although, at small abundances <10⁻¹⁴ for the latter three)

Hydrocarbon shielding and prebiotic chemistry in exoplanet atmospheres

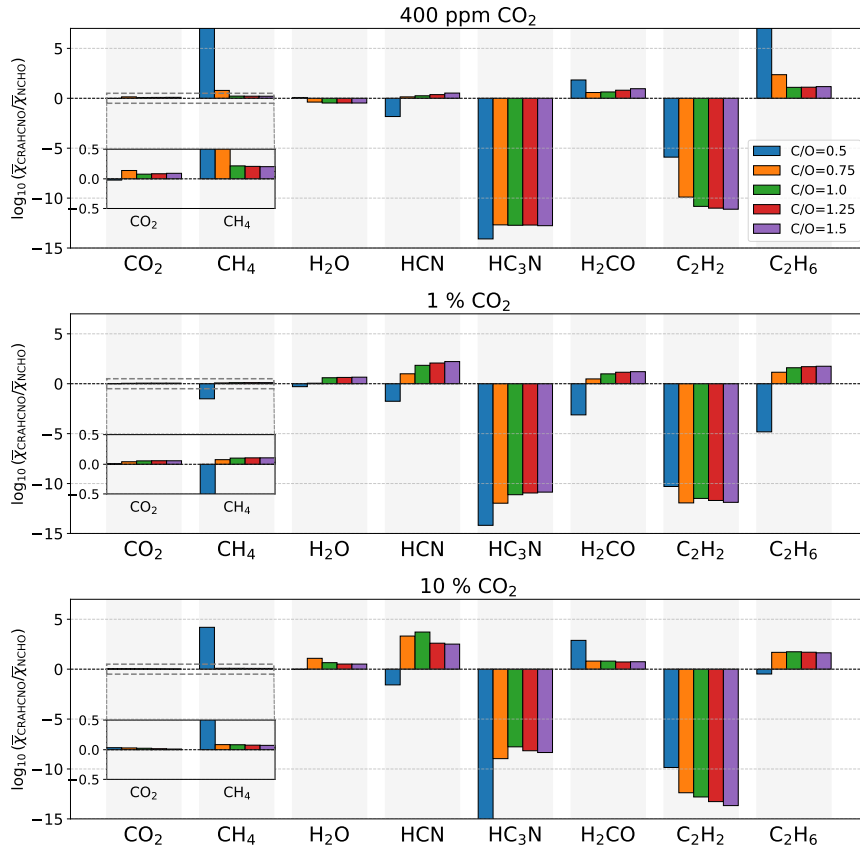


Figure 6: Ratios of vertically averaged mixing ratios (χ) from simulations with CRAHCN-O versus N-C-H-O, for 400 ppm CO₂ (top), 1% (middle), and 10% CO₂ (bottom). For each species, we compute the difference as a function of C/O ratio as specified in Table 1.

shows that the pathways to feedstock molecules in the absence of CH₄ are faster in N-C-H-O. Lastly, H₂O forms in the upper atmosphere from photochemical products of CH₄ for CRAHCN-O, provided that sufficient CH₄ is present. This explains why the enhancement in CRAHCN-O is seen for the 1% and 10% cases and not for 400 ppm case.

For 1% CO₂, increasing C₂H₆ abundances as a function of C/O with the CRAHCN-O network strengthens the photochemical shielding. C₂H₆ abundances increase more moderately with the N-C-H-O network, which causes the enhanced inter-network differences with the C/O ratio in Figure 6. On the other hand, for 10% CO₂, C₂H₆ formation saturates in CRAHCN-O for a C/O ratio between 0.75 and 1.0, which can be seen in Figure 3f with peak abundances of C₂H₆ already reaching the top of the atmosphere. With N-C-H-O, C₂H₆ increases are stronger with C/O ratio (Figure 5), leading to decreased inter-network differences. These contrasting trends are reflected in the distribution of inter-network differences of HCN and H₂O due to the shielding effects. Hence, even though the reactions included in each network do not change, the resulting inter-network differences still fundamentally depend on the background scenario.

Despite distinct spectral energy distributions for other M-type stars (see Figure 1), the trends with C/O ratio persist, as shown for the 1% CO₂ cases in Figure 7. For C/O=0.5, we note the same findings as before that 1) CO₂ and H₂O are similar, 2) CH₄, C₂H₂, C₂H₆, and H₂CO have large inter-network ratios reflecting their negligible abundances, and 3) HCN consistently forms more efficiently in N-C-H-O. For C/O>0.5, C₂H₆ starts to accumulate in CRAHCN-O and similarly shields CO₂, CH₄, HCN, H₂CO. Nevertheless, with N-C-H-O, the location of the UV photosphere between 115–145 nm shifts to lower pressures for GJ 676 A and GJ 436 and higher pressures for TRAPPIST-1 (not shown), due to lower (GJ 676 A and GJ 436) and higher (TRAPPIST-1) stellar fluxes in this wavelength range. The photosphere shifts are similar for CRAHCN-O. Lastly, the pathways to HC₃N and C₂H₂ are again slow in CRAHCN-O. Importantly,

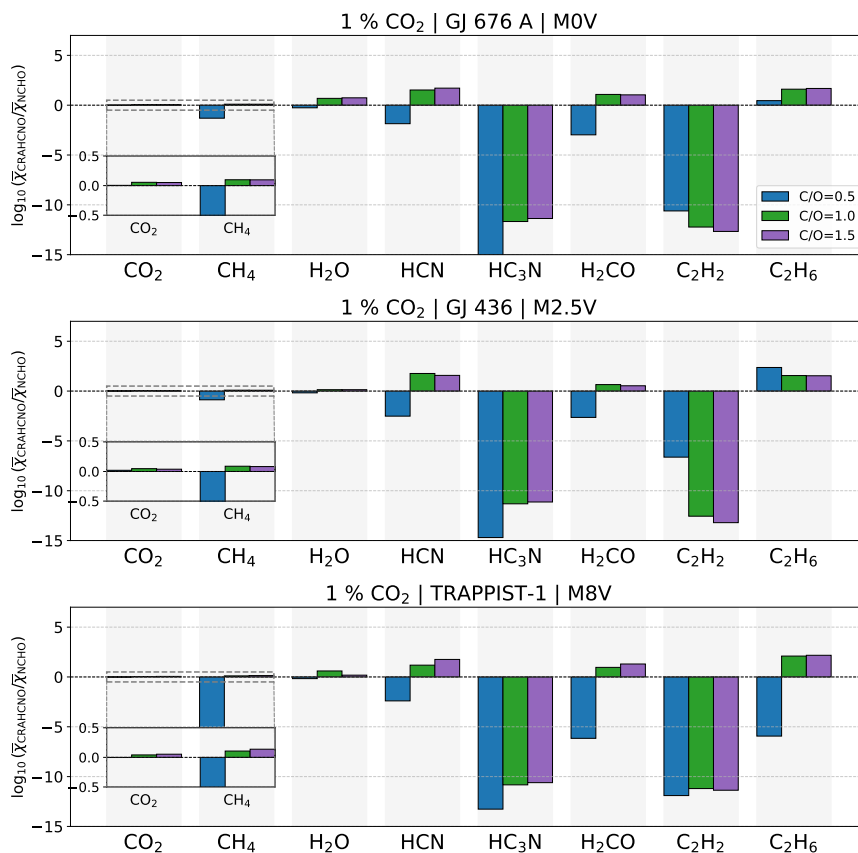


Figure 7: Ratios of vertically averaged mixing ratios (χ) from simulations with CRAHCN-O versus N-C-H-O for the 1% CO₂ case, assuming distinct host star spectral energy distributions (see Figure 1a). We only include C/O ratios of 0.5, 1.0, and 1.5 from Table 1 to see if the trends persist for different M stars.

by considering the irradiance from distinct M0V, M2.5V, M5.5V, and M8V stars, we show that the photochemical shielding effects associated with C₂H₆ accumulation in CRAHCN-O apply to planets orbiting distinct M-type stars.

3.3. Pathway analyses

In this Section, we present the dominant reaction rates (both production and destruction) and the dominant pathways to form feedstock molecules and hydrocarbons from the initial species, to identify the causes of inter-network differences between VULCAN/N-C-H-O and VULCAN/CRAHCN-O. We include the pathways to nitriles (HCN, HC₃N), an aldehyde (H₂CO), and a subset of hydrocarbons (C₂H₂, C₂H₆, C₃H₄, C₄H₃, C₆H₅). By comparing all reactions involving a given species, the dominant reactions are those with the fastest rates. The pathway analysis identifies all the reaction steps and the rate-limiting step in the shortest path between two species, as described in Section 2.3. For brevity, we focus on the results for the 1% CO₂ case, but note that the same reaction rates were used in the other simulations. Thus, the results presented here apply more generally, albeit with a different pressure dependence since the UV photosphere moves to higher (400 ppm CO₂) or lower (10% CO₂ case) pressures. At the end of the Section, we summarise and compare the rate coefficients for the most important bimolecular and termolecular reactions in Tables 3 and 4, respectively.

3.3.1. Nitriles

For C/O=0.5, N-C-H-O has non-zero reaction rates of HCN production at all pressure levels, as we can see from the vertical distribution in Figure 8a. Net production regions are seen at low $P < 10^{-6}$ bar and at high $P > 4 \times 10^{-4}$ bar. For CRAHCN-O, we see production of HCN at low pressures ($< 10^{-6}$ bar) but not substantially at high pressures (Figure 8b). We investigate the pathways from N₂, CO₂, and H₂O to HCN, due to the absence of CH₄ in the C/O=0.5

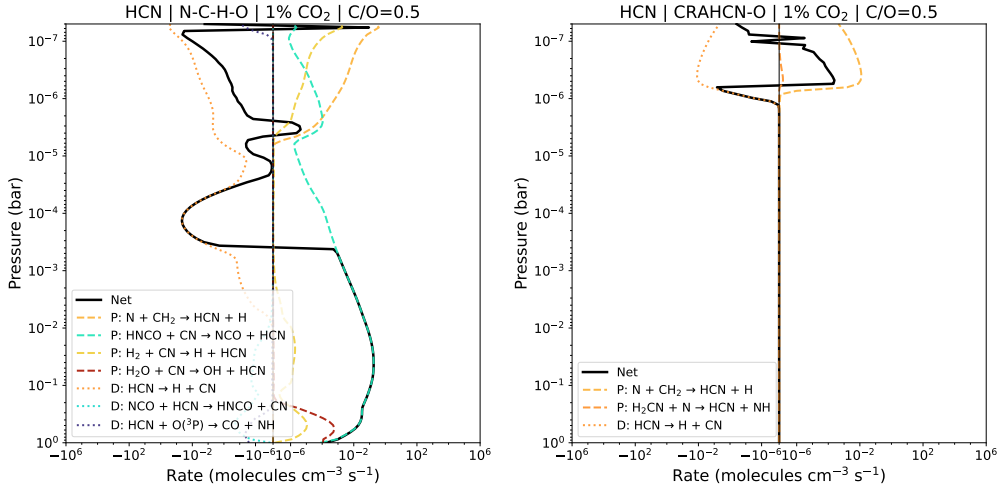


Figure 8: Reaction rates for the dominant CO₂ reactions involving HCN in the 1% CO₂ case, for C/O=0.5 and comparing N-C-H-O (a) and CRAHCN-O (b). The dashed lines represent production reactions, the dotted lines destruction reactions. The net rate shows the difference between all production and all destruction reactions. Reaction colours agree across panels.

setups. In Figure 9, we split the pathways for N-C-H-O into a low-pressure (10⁻⁷ bar) and high-pressure (10⁻¹ bar) region. For low pressures, N-C-H-O forms HCN most efficiently via:



Reaction R2 forms the rate-limiting step. H₂O and CO₂ photolysis provide CH and thus CH₂ for Reaction R2. For high pressures, there is a pathway starting from CO₂:



In this pathway, Reaction R5 is the rate-limiting step. The CN and H₂ required in this pathway come from the upper atmosphere following photolysis of N₂, CO₂, and H₂O. In CRAHCN-O, the absence of HNCO means the high-pressure pathway does not occur. The pathway from N₂ is the same as in N-C-H-O (Reactions R1 and R2), as shown in Figure 9. Again, H₂O photolysis at higher pressures followed by mixing instead provides H for the production of CH₂ in Reaction R2. The absorption cross sections for reaction R1 are identical, but the rate coefficients associated with R2 are different (see Table 3). The rate constants at 298 K (k_{298}) are similar, but k in CRAHCN-O becomes an order of magnitude smaller with decreasing temperature. Although not shown here for brevity, the pathway differences between both networks are the same for the 400 ppm and 10% CO₂ cases, but with the key pathways shifted to higher and lower pressures, respectively. The pressure shift is due to shielding effects, like in Figure 4.

For C/O>0.5, HCN production through reactions R1 and R2 still occurs close to the top of the atmosphere with N-C-H-O (Figure 10a and 11). Considering the 1% CO₂ case at C/O=1.5, the net HCN production in N-C-H-O peaks around 7×10⁻⁶ bar and remains high for increasing pressures, being dominated by the pathway involving HCNO. The pathway includes Reactions 3 and 5, but HNCO formation is now dominated by HCO:



as shown in Figure 11. With increasing CO₂ and CH₄ abundances, the HNCO production regions shift to lower pressures. The lower availability of HNCO then affect the HCN abundances at higher pressures ($P > 10^{-4}$ for the

Hydrocarbon shielding and prebiotic chemistry in exoplanet atmospheres

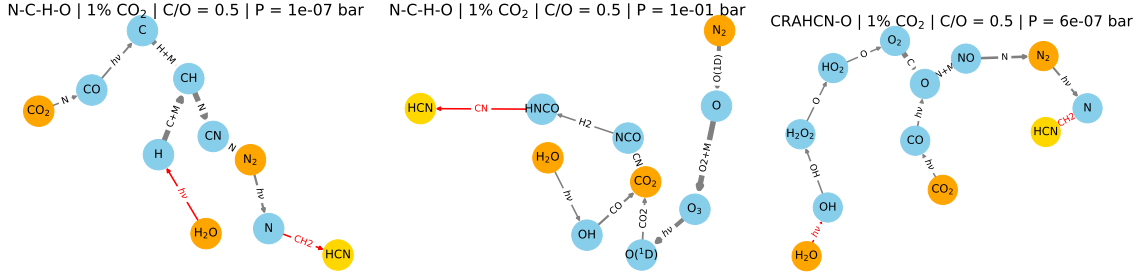
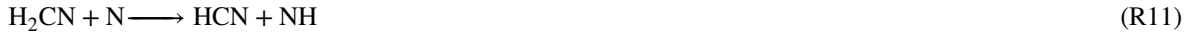


Figure 9: Dominant pathways to HCN formation for the N-C-H-O network at 10^{-7} and 10^{-1} bar and CRAHCN-O at 6×10^{-7} bar, as indicated by the titles. Pathways are shown for the 1% CO_2 case at $\text{C/O}=0.5$. Initialisation species are shown in orange, the target species (in this case, HCN) in yellow, and intermediate species in blue. The other reactant species involved in reaching the next node in a pathway are shown as edge labels. Edge widths represent reaction rates, with wider edges indicating faster reactions; the rate-limiting step is shown in red.

400 ppm case, $>10^{-5}$ for the 1% case, $>10^{-6}$ bar for the 10% case), explaining why HCN abundances are higher in N-C-H-O than CRAHCN-O for 400 ppm CO_2 but not for 1% and 10% CO_2 (see Figure 3). Although not shown in Figure 11 for N-C-H-O, pathways involving H_2CN then become more dominant. HCN forms at low pressures through:



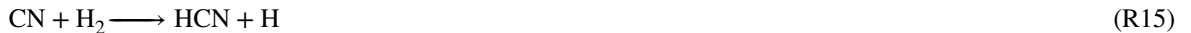
Reaction R9 is the rate-limiting step. In CRAHCN-O, one of the low-pressure (6×10^{-8} bar) pathways again consists of Reactions R1 and R2, as shown in Figure 11. CH_4 photolysis initiates another important pathway through Reactions R8 and R9, followed by:



Note that CH_3 formation also occurs through the oxidation of CH_4 :

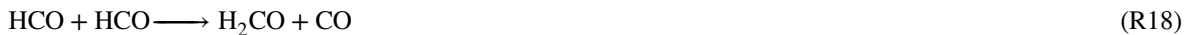


For low pressures, we find another pathway to HCN from CH_4 (not shown in Figure 11):



Reaction R15 is the rate-limiting step and $\text{CH}_2({}^1\text{A}_1)$ represents the first excited singlet state of CH_2 .

Prominent net production of HCN is also seen around 7×10^{-7} bar, involving H_2CO as intermediate species:



Reaction R19 is the rate-limiting step. Note that the fast HCO formation through R17 is the important distinction between the networks for this pathway. The high HCO abundances also regenerate CO_2 in the upper atmosphere of the 400 ppm case (see Figure 3). For both N-C-H-O and CRAHCN-O, the direct pathway becomes dominant and rate-limiting at high pressures:



Hydrocarbon shielding and prebiotic chemistry in exoplanet atmospheres

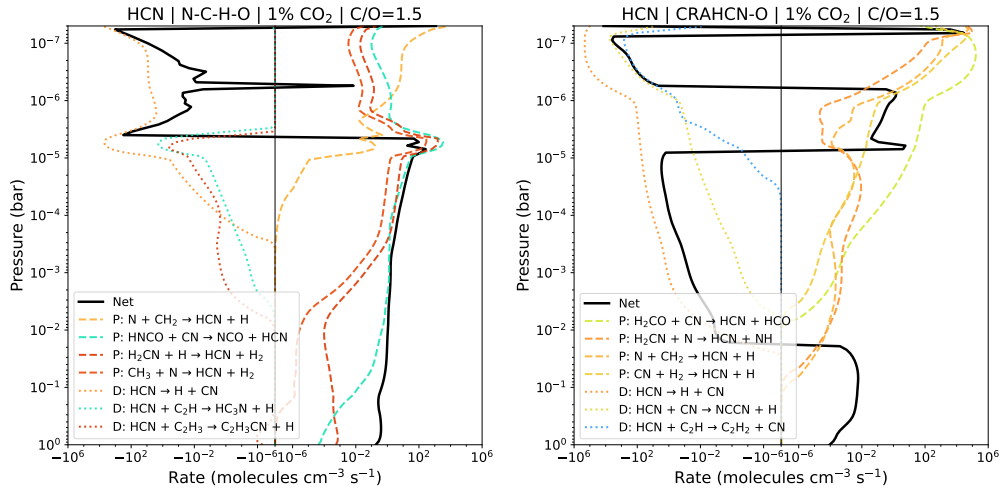


Figure 10: Same as Figure 8, but for the 1% CO₂ case at C/O=1.5.

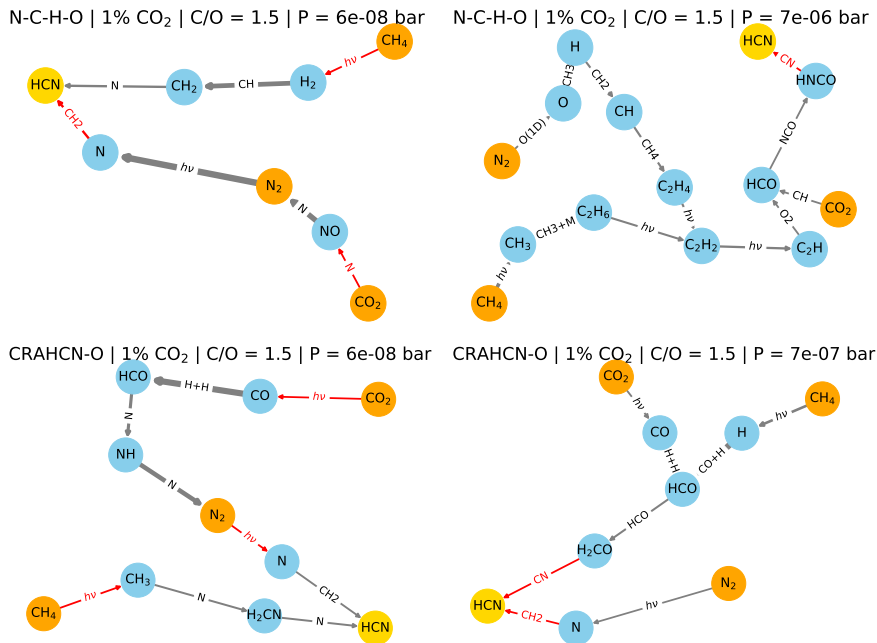


Figure 11: Same as Figure 9, but for the 1% CO₂ case at C/O=1.5.

With increasing CH₄ abundances, Reaction R20 starts to dominate a larger vertical extent of the atmosphere (not shown).

HC₃N formation is much more efficient in the N-C-H-O network. For N-C-H-O, its net production is strongest for low pressures (<10⁻⁴ bar, see Figure 12a) and depends on hydrocarbon availability. As shown in Figure 13, the dominant upper atmosphere pathways trace back to CH₄ photolysis via Reaction R14 followed by:



Hydrocarbon shielding and prebiotic chemistry in exoplanet atmospheres

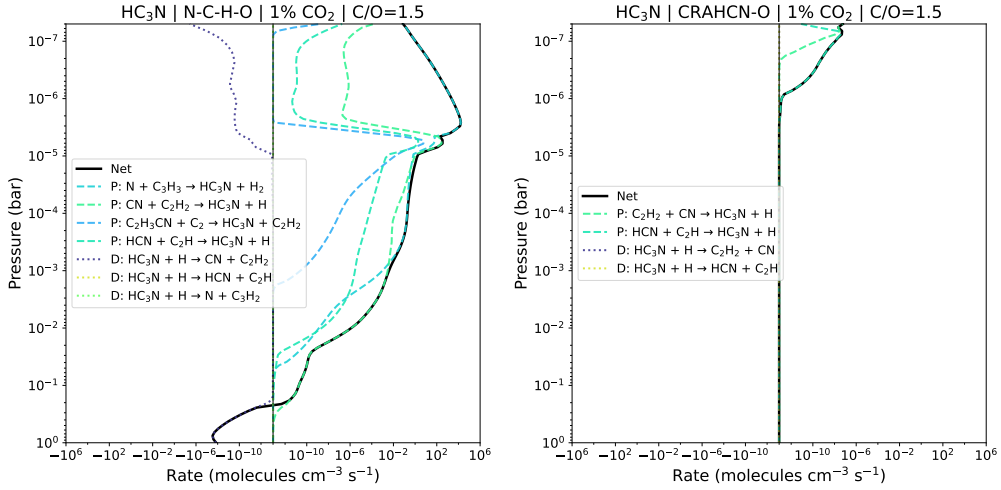


Figure 12: Same as Figure 8, but showing the dominant rates controlling HC_3N in the 1% CO_2 case at $\text{C}/\text{O}=1.5$.

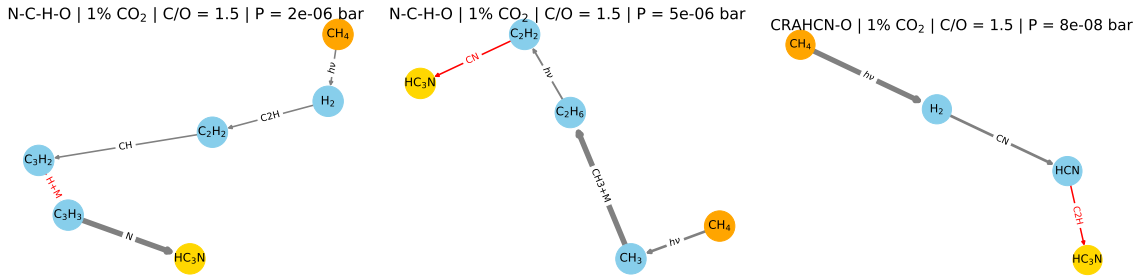


Figure 13: Same as Figure 9, but showing the dominant pathways to HC_3N for the 1% CO_2 case at $\text{C}/\text{O}=1.5$.



Around 5×10^{-6} bar, CH_4 photolysis via Reaction R8 initiates a second important pathway:



The rate-limiting steps in these pathways are Reactions R23 and R27, respectively.

Figure 12b shows that HC_3N forms in CRAHCN-O with Reaction R27 as the rate-limiting step, but the process is slower due to low C_2H_2 abundance, as discussed in Section 3.3.3. The other pathway to HC_3N involves HCN formation as described in Section 3.3.1 and the rate-limiting step:



CRAHCN-O predicts relatively low C_2H abundances, similar to C_2H_2 , which makes this reaction slow. Hence, a clear difference between the networks is caused by the dominant role of hydrocarbons in HC_3N formation. Note that CRAHCN-O was not necessarily built to comprehensively simulate HC_3N formation, so distinct HC_3N profiles between the networks are not unexpected.

3.3.2. Formaldehyde

The formation of H_2CO traces back to both CH_4 and CO_2 . The net rates in Figure 14 include strong peaks for both networks, although their vertical distributions differ due to the shielding effects in CRAHCN-O and network

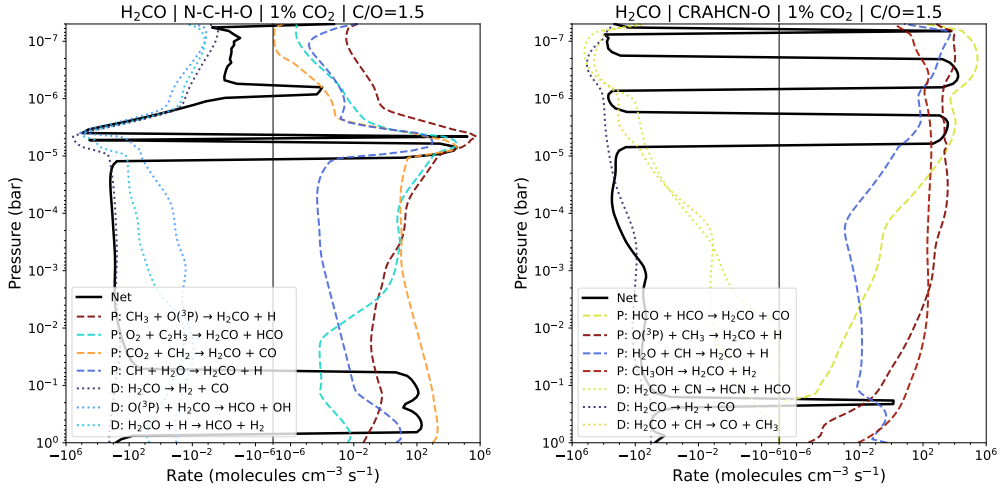


Figure 14: Same as Figure 8, but showing the dominant rates controlling H_2CO in the 1% CO_2 case at $\text{C}/\text{O}=1.5$.

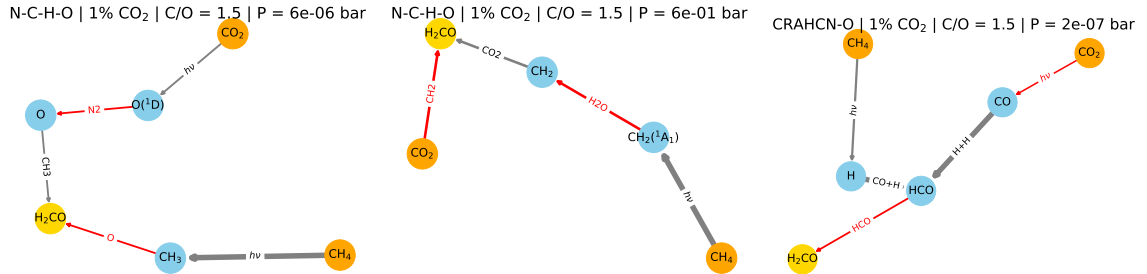


Figure 15: Same as Figure 9, but showing the dominant pathways to H_2CO for the 1% CO_2 case at $\text{C}/\text{O}=1.5$.

differences. The strongest peak in N-C-H-O involves CH_3 ($\sim 6 \times 10^{-6}$ bar), whereas the self-reaction of HCO dominates the strongest peaks in CRAHCN-O ($< 10^{-5}$ bar). For N-C-H-O, the most important pathways to H_2CO are represented by four reactions, as shown in Figure 15, and start with CH_4 (Reaction R8) and CO_2 (Reaction R16) photolysis followed by:



Importantly, net production of H_2CO is also predicted at high pressures ($> 10^{-1}$ bar) by N-C-H-O (Figure 14a), through a pathway that involves CH_4 photolysis via Reaction R14 and CO_2 :



This pathway scales with background CO_2 and CH_4 levels, as it is less efficient for the 400 ppm CO_2 cases. For H_2CO formation, Reactions R29 and R31 are the rate-limiting steps. In CRAHCN-O, H_2CO formation in the main net production peaks is dominated by the presence of HCO, which is formed through Reactions R16, R17 and R18 as the rate-limiting step.

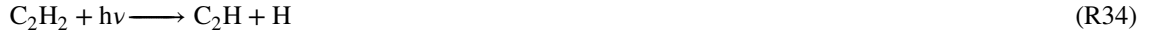
3.3.3. Hydrocarbons

The dominant production pathways of hydrocarbons like C_2H_2 , C_2H_6 , and C_4H_3 in the N-C-H-O network are found at the same pressure levels as the peaks in their abundance profiles in Figure 3. For the 1% CO_2 case at $\text{C}/\text{O}=1.5$, this

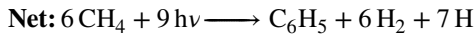
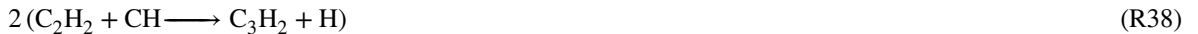
corresponds to $\sim 7 \times 10^{-6}$ bar, as can also be seen in panels a and c of Figure 16. In N-C-H-O, C_2H_2 predominantly forms from the photolysis of C_2H_6 , meaning that the dominant production pathways are shared. The other production and destruction reactions show that other hydrocarbons (e.g., C_2H_4 , C_2H_5 , C_2H , C_4H_2 , C_3H_4) are closely related to the abundances of C_2H_2 and C_2H_6 . Figure 17 summarizes the pathways at a pressure of $\sim 7 \times 10^{-6}$ bar and how they trace back to CH_4 . Importantly, N-C-H-O accumulates the final nodes in these pathways, being C_3H_4 , C_4H_3 , and C_6H_5 . Since the production of most hydrocarbons centres around the same pressure region, it is straightforward to construct a complete chemical mechanism from the pathway analysis for a simpler comparison between both networks and derive the net reactions. First, C_3H_4 traces back to the photolysis of CH_4 through two different channels:



As shown in Figure 17, the rate-limiting steps include Reactions R8 for C_2H_6 , R26 for C_2H_2 , and R33 for C_3H_4 . C_4H_3 is formed from photolysis of multiple CH_4 molecules in a single channel:



The rate-limiting step for C_4H_3 is Reaction R36. The same photolysis channel of CH_4 and a third channel drive the formation of C_6H_5 and C_6H_6 :



The rate-limiting steps are Reaction R39 for C_6H_6 and R40 for C_6H_5 . The four net reactions above then summarise the photochemical buildup of hydrocarbons in the N-C-H-O network. Another important pathway to C_2H_2 is initiated by CH_4 photolysis to CH (Reaction R37) and involves C_2H_4 as an intermediate species:



The dominant destruction pathway for C_3H_4 at all pressure levels and initial conditions forms C_2H_2 again (not shown):



However, formation reactions are persistently faster than destruction ones, thus promoting C_3H_4 accumulation in N-C-H-O. C_4H_3 destruction leads to the most complex hydrocarbons in the network (C_6H_5 and C_6H_6):

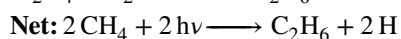
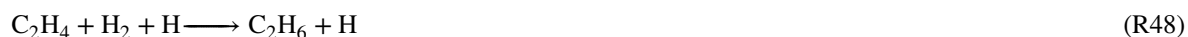


Again, the balance between reaction strengths strongly favours C_4H_3 accumulation. Additionally, C_3H_3 can directly form C_3H_4 :

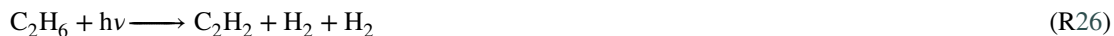


Since the pathways to C_6H_5 and C_6H_6 are slower, C_4H_3 and C_3H_4 end up as the most abundant hydrocarbon reservoirs in N-C-H-O. As mentioned in Section 3.1 and shown in Appendix Figure 20, C_4H_3 abundances are about an order of magnitude higher than C_3H_4 , illustrating the preferential formation of C_4H_3 due to atomic H (relatively abundant at low pressures) driving its rate-limiting step (Reaction R36).

For CRAHCN-O, C_2H_2 and C_2H_6 production again show a peak as a function of pressure ($\sim 3 \times 10^{-7}$ bar, see Figure 16b). At this pressure level, we can construct a chemical mechanism for C_2H_6 formation based on the pathways in Figure 17:



If we keep the five reactions of this mechanism and add the cycle introduced by C_2H_6 destruction twice, we find that C_2H_6 is formed along with one of its precursors:



This CH_3 can again be used for C_2H_6 production through Reaction R25. However, the tendency to accumulate C_2H_6 is mainly due to the imbalance in reaction rates in the cycle between C_2H_4 , C_2H_6 , and C_2H_2 as shown by the width of the edges in Figure 17. The wider edge of Reaction R48 shows that it is faster than Reactions R26 and R49 and illustrates how the cycle can lead to an accumulation of C_2H_6 . This mechanism subsequently causes the substantial photochemical shielding by C_2H_6 in CRAHCN-O, further affecting other feedstock molecules. Ultimately, the extent and effects of the C_2H_6 accumulation in CRAHCN-O are due to the absence of pathways to more complex hydrocarbons like those in N-C-H-O.

For pressures $> 10^{-4}$ bar, we also see inter-network differences in the net rates in Figure 16, where C_2H_6 formation in N-C-H-O is dominated by Reaction R25 and in CRAHCN-O by Reaction R48 and at the highest pressures by:



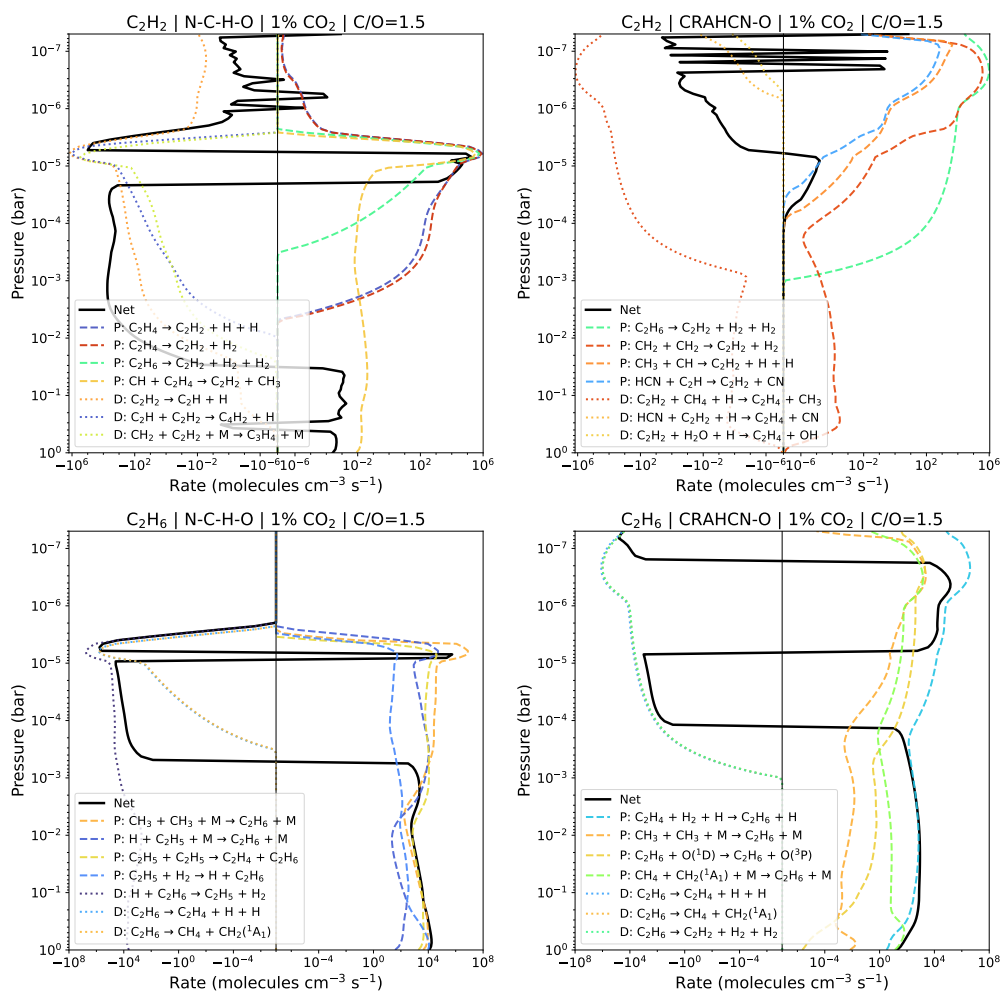


Figure 16: Same as Figure 8, but showing the dominant rates controlling C_2H_2 and C_2H_6 in the 1% CO_2 case at $C/O=1.5$.

These partially explain the differences in C_2H_6 abundances at higher pressures, along with vertical mixing from the peak production regions. Unlike C_2H_6 , net production of C_2H_2 is negligible at $>10^{-4}$ bar in both networks (Figure 16). Therefore, the tropospheric abundances of C_2H_2 and its derivatives (e.g., C_3H_4 , C_4H_3 , C_6H_5 , C_6H_6) strongly depend on vertical mixing from the photochemical production regions in the upper atmosphere. This has profound implications for the predicted tropospheric abundances with the N-C-H-O network. With increasing CO_2 and CH_4 levels, the production regions shift to lower pressures, making it harder for mixing processes to reach the troposphere by crossing the mixing barrier presented by the tropopause ($\sim 10^{-1}$ bar in Figure 1). Therefore, with increasing CO_2 and CH_4 levels, the photochemically produced C_2H_2 and C_4H_3 start to disappear from the troposphere, as we see for the 10% CO_2 cases in Figure 3f and i. The same reasoning explains the absence of HCN and HC_3N in the troposphere for the high CO_2 and CH_4 scenarios. Since pathways at high pressures still exist for C_2H_6 (Reaction R25) as well as H_2CO (Reaction R32), their tropospheric abundances are less affected by this inability of vertical mixing to transport the photochemical products down to higher pressures.

4. Discussion and Conclusion

4.1. Hydrocarbon complexity

Our study highlights the strong influence of hydrocarbon complexity on the simulated abundances of feedstock molecules in exoplanet atmospheres. The photochemical environment depends critically on which hydrocarbons

Hydrocarbon shielding and prebiotic chemistry in exoplanet atmospheres

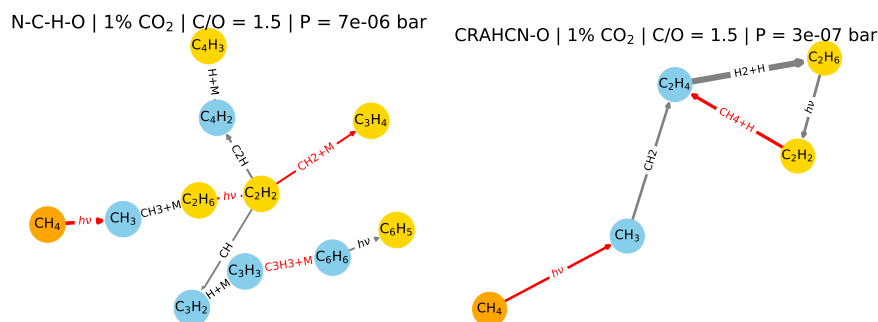


Figure 17: Same as Figure 9, but showing the dominant pathways to hydrocarbons for the 1% CO₂ case at C/O=1.5.

accumulate and how effectively they provide photochemical shielding. Current photochemical models are restricted by the availability and accuracy of kinetic data for thermochemical reactions and absorption cross-section data for photodissociation reactions. Developing a framework to evaluate their coupled impacts on further chemical processes is therefore essential.

We perform three additional tests focused on the shielding effects of hydrocarbons, shown in Figure 18. First, we follow Lavvas et al. (2008) and estimate the photolysis of C₃H₄ into C₃H₃ and C₃H₂, with branching ratios of 0.64 and 0.36, respectively, and cross-section data from Palmer et al. (1999). Unable to find cross-section data for C₄H₃, we used the same cross sections and consider only the destruction into C₃H₃. The inclusion of C₃H₄ and C₄H₃ photolysis adds photochemical shielding to N-C-H-O, protecting CH₄ and CO₂ abundances to lower pressures and bringing them closer to CRAHCN-O (Figure 18a). The HCN profile also moves closer to that in CRAHCN-O. As a second test, we added artificial destruction reactions from C₂H₆ to C₃H₄ and C₄H₃ into CRAHCN-O, without treating the latter two as photochemically active. This decreases the C₂H₆ shielding effects, bringing photochemical destruction of CH₄ and CO₂ to higher pressures (Figure 18b). Already, this simple artificial C₂H₆ destruction brings HCN and C₄H₃ remarkably close to the profiles predicted by N-C-H-O. Lastly, we switch off all photodissociation channels of C₂H₆ in CRAHCN-O. Again, the HCN profile moves towards that of N-C-H-O and shielding of CH₄ and CO₂ also visibly weakens (Figure 18c). Since C₄H₃ is a radical species, its accumulation is not expected chemically, highlighting the need to expand on the hydrocarbon chemistry. A comprehensive reconciliation is beyond the scope of this paper, but will be attempted as part of future work that builds upon the key pathways presented here. As the lack of C₄H₃ cross-section data demonstrates, for many of the higher-order hydrocarbon reactions, we need more measurements of rate coefficients, thermodynamic data (for reversing reactions), and cross sections.

Previous studies have investigated the atmospheres of Titan-like exoplanets (N₂-dominated with ~1.4% CH₄), including hydrocarbons. Lora et al. (2018) explored both atmospheric circulation and photochemistry, whilst incorporating hydrocarbons up to C₆ species. Their predictions of peak C₂H₆ abundances at 10⁻⁷–10⁻⁸ bar and increasing HCN abundances (see Figure 6 in Lora et al., 2018) agree with CRAHCN-O profiles the 1% and 10% CO₂ cases. C₂H₆ abundances from Lora et al. (2018) are considerably lower, but compensated by C₂H₂ and C₂H₄ at mixing ratios of 10⁻³. We note that our atmospheres are much warmer than the Titan-like exoplanets in Lora et al. (2018); Adams et al. (2022) and are on the order of early Earth and similar exoplanets (e.g., Arney et al., 2016, 2017). Likely due to the warmer temperatures, reaction rates in our work are 1-2 orders of magnitude faster than in Lora et al. (2018). We also note that our simulations contain substantial CO₂, unlike those of Lora et al. (2018). Their upper atmospheric boundary is at lower pressures (10⁻¹¹ bar), warranting detailed studies of the effects of upper boundary choices. The pathways to C₂H₆ are similarly dominated by Reaction R25, with Reaction R9 competing to form nitriles instead. Adams et al. (2022) expand the study of Titan-like atmospheres around different stars by considering close-in orbits and H₂-dominated atmospheres. Similarly, nitriles and hydrocarbons exhibit high mixing ratios in the upper atmosphere for Titan-like conditions, agreeing with our results using CRAHCN-O. For warmer atmospheres and for H₂-dominated conditions, CH₃ recycles back into CH₄ due to reactions with H in the upper atmosphere. Instead, CH₂ and CH are the main CH₄ sinks, and hydrocarbons do not accumulate at low pressures. At higher pressures, CH₃ forms to promote the formation of hydrocarbons and nitriles (Adams et al., 2022). This is in better agreement with our N-C-H-O results.

Table 3

Key bimolecular reactions in the pathways to feedstock molecules, comparing N-C-H-O and CRAHCN-O. We provide the rate coefficients A , b , and E_a as well as the rate at 298 K (k_{298}). Note that similar rates at 298 K do not guarantee agreement at lower temperatures relevant to the simulated atmosphere (see Figure 1). In the final column, we recommend using the rate coefficients from CRAHCN-O (C), N-C-H-O (N), or further measurements (M). The three blocks split the reactions controlling nitriles, formaldehyde, and hydrocarbons.

R	Reaction	$[A \text{ (cm}^3\text{s}^{-1}), b, E_a \text{ (K)}]$		$k_{298} \text{ (cm}^3\text{s}^{-1})$		Rec.
		CRAHCN-O	N-C-H-O	CRAHCN-O	N-C-H-O	
R2	$\text{N} + \text{CH}_2 \longrightarrow \text{HCN} + \text{H}$	[1e-10, 0, 0]	[4.3e-10, 0, 420]	1.0e-10	1.05e-10	M
R3	$\text{CN} + \text{CO}_2 \longrightarrow \text{CO} + \text{NCO}$	[N/A]	[6.14e-12, 0, 0]	N/A	6.14e-12	M
R4	$\text{HNCO} + \text{H} \longrightarrow \text{NCO} + \text{H}_2$	[N/A]	[2.91e-19, 2.41, 6190]	N/A	2.54e-22	N
R5	$\text{NCO} + \text{HCN} \longrightarrow \text{HNCO} + \text{CN}$	[N/A]	[2.01e-11, 0, 4460]	N/A	6.36e-18	M
R7	$\text{NCO} + \text{HCO} \longrightarrow \text{HNCO} + \text{CO}$	[N/A]	[5.99e-11, 0, 0]	N/A	5.99e-11	M
R9	$\text{CH}_3 + \text{N} \longrightarrow \text{H}_2\text{CN} + \text{H}$	[7.7e-11, 0, 0]	[1.01e-9, -0.31, 145]	7.7e-11	1.06e-10	C
R11	$\text{H}_2\text{CN} + \text{N} \longrightarrow \text{HCN} + \text{NH}$	[1e-10, 0, 200]	[N/A]	5.11e-11	N/A	C
R19	$\text{H}_2\text{CO} + \text{CN} \longrightarrow \text{HCN} + \text{HCO}$	[2.74e-19, 2.72, -718]	[N/A]	1.64e-11	N/A	M
R15	$\text{CN} + \text{H}_2 \longrightarrow \text{HCN} + \text{H}$	[5.93e-16, 1.55, 1510]	[5.99e-16, 1.55, 1510]	2.56e-14	2.58e-14	-
R20	$\text{CH}_4 + \text{CN} \longrightarrow \text{HCN} + \text{CH}_3$	[1.50e-11, 0, 940.0]	[1.50e-19, 2.64, -150]	6.40e-13	8.45e-13	C
R24	$\text{N} + \text{C}_3\text{H}_3 \longrightarrow \text{HC}_3\text{N} + \text{H}$	[N/A]	[5.00e-11, 0, 0]	N/A	5.00e-11	M
R27	$\text{CN} + \text{C}_2\text{H}_2 \longrightarrow \text{HC}_3\text{N} + \text{H}$	[2.27e-10, 0, 0]	[2.27e-10, 0, 0]	2.27e-10	2.27e-10	-
R28	$\text{HCN} + \text{C}_2\text{H} \longrightarrow \text{HC}_3\text{N} + \text{H}$	[5.30e-12, 0, 768.4]	[5.30e-12, 0, 769]	4.02e-13	4.01e-13	M
R12	$\text{CH}_4 + \text{OH} \longrightarrow \text{H}_2\text{O} + \text{CH}_3$	[2.58e-17, 1.83, 1396]	[1.68e-18, 2.18, 1231]	8.03e-15	6.68e-15	-
R13	$\text{CH}_4 + \text{O}(^1\text{D}) \longrightarrow \text{OH} + \text{CH}_3$	[2.2e-10, 0, 0]	[1.13e-10, 0, 0]	2.2e-10	1.13e-10	M
R17	$\text{HCO} + \text{H} \longrightarrow \text{CO} + \text{H} + \text{H}$	[2.4e-11, 0, 0]	[N/A]	2.4e-11	N/A	M
R18	$\text{HCO} + \text{HCO} \longrightarrow \text{H}_2\text{CO} + \text{CO}$	[4.20e-11, 0, 0]	[3.01e-11, 0, 0]	4.2e-11	3.01e-11	-
R29	$\text{O}(^1\text{D}) + \text{N}_2 \longrightarrow \text{O}(^3\text{P}) + \text{N}_2$	[N/A]	[1.79E-11, 0, -107]	N/A	2.56e-11	N
R30	$\text{CH}_3 + \text{O}(^3\text{P}) \longrightarrow \text{H}_2\text{CO} + \text{H}$	[1.40e-10, 0, 0]	[1.40e-10, 0, 0]	1.40e-10	1.40e-10	-
R31	$\text{CH}_2(^1\text{A}_1) + \text{H}_2\text{O} \longrightarrow \text{CH}_2 + \text{H}_2\text{O}$	[N/A]	[5.0e-11, 0, 0]	N/A	5.0e-11	N
R32	$\text{CH}_2 + \text{CO}_2 \longrightarrow \text{H}_2\text{CO} + \text{CO}$	[N/A]	[3.90e-14, 0, 0]	N/A	3.9e-14	M
R22	$\text{CH} + \text{C}_2\text{H}_2 \longrightarrow \text{C}_3\text{H}_2 + \text{H}$	[N/A]	[1.5e-10, 0, -252]	N/A	3.49e-10	N
R35	$\text{C}_2\text{H} + \text{C}_2\text{H}_2 \longrightarrow \text{C}_4\text{H}_2 + \text{H}$	[N/A]	[3.18e-11, 0.24, -37]	N/A	1.41e-10	N
R41	$\text{CH} + \text{CH}_4 \longrightarrow \text{H} + \text{C}_2\text{H}_4$	[9.8e-11, 0, 0]	[5e-11, 0, -200]	9.8e-11	9.78e-11	N
R43	$\text{CH}_3 + \text{C}_2\text{H}_2 \longrightarrow \text{C}_3\text{H}_4 + \text{H}$	[N/A]	[8.57e-15, 0.86, 11100]	N/A	7.66e-29	M
R47	$\text{CH}_3 + \text{CH}_2 \longrightarrow \text{C}_2\text{H}_4 + \text{H}$	[7e-11, 0, 0]	[7.01e-11, 0, 0]	7e-11	7.01e-11	-
R48	$\text{C}_2\text{H}_6 + \text{H} \longrightarrow \text{C}_2\text{H}_5 + \text{H}_2$ $\longrightarrow \text{C}_2\text{H}_4 + \text{H}_2 + \text{H}$	[2.39e-15, 1.5, 3730]	[9.19E-22, 3.5, 2600]	6.11e-16	6.82e-17	M
R49	$\text{C}_2\text{H}_4 + \text{CH}_3 \longrightarrow \text{C}_2\text{H}_3 + \text{CH}_4$ $\longrightarrow \text{C}_2\text{H}_2 + \text{CH}_4 + \text{H}$	[6.91e-12, 0, 5599]	[N/A]	4.78e-20	N/A	M

References and notes: R2: Pearce et al. (2019); estimated by Tsai et al. (2021), R3: Haynes et al. (1975), R4: Inverse; Nguyen et al. (1996), R5: Inverse; Tsang (1992), R7: Tsang & Herron (1991), R9: Pearce et al. (2020b); Davidson & Hanson (1991); Dean & Bozzelli (2000), R11: Nesbitt et al. (1990), R19: Yu et al. (1993), R15: Tsang (1992), R20: Baulch et al. (1992); Baulch et al. (1994), R24: Loison et al. (2017), R27: Gannon et al. (2007), R28: Hoobler & Leone (1997), R12: Baulch et al. (1992); Srinivasan et al. (2005), R13: Pearce et al. (2020a); Demore et al. (1994), R17: Inverse; Pearce et al. (2020a), R18: Pearce et al. (2020a); Tsang & Hampson (1986), R29: Atkinson et al. (1997), R30: Baulch et al. (1992), R31: Wang & Frenklach (1997), R32: Tsang & Hampson (1986), R22: Guadagnini et al. (1998), R41: Berman & Lin (1983); Baulch et al. (1992), R35: Eiteneer & Frenklach (2003), R43: Inverse; Davis et al. (1999), R47: Baulch et al. (1992), R48: Inverse; Baulch et al. (1992), C2H6 + H \rightarrow C2H5 + H2: Inverse; Tsang & Hampson (1986), R49: Inverse; Baulch et al. (1992).

A hydrocarbon shielding mechanism for Early Earth was discovered by Yoshida et al. (2024), showing how C_2H_2 and C_3H_4 isomers (CH_2CCH_2 , allene and $\text{CH}_3\text{C}_2\text{H}$, propyne) suppress H_2O photolysis, producing fewer oxidants and thus enhancing the production of feedstock molecules. Their chemical network includes hydrocarbons up to C3 and predicts substantial C_2H_6 abundances. However, the cross-sections of C_2H_6 fall below those of CH_2CCH_2 and $\text{CH}_3\text{C}_2\text{H}$ (Yoshida et al., 2024), emphasising the potential shielding role of C_3H_4 isomers. In N-C-H-O, C_3H_4 represents CH_2CCH_2 , and we also demonstrate its shielding effect on predicted N-C-H-O abundances in Figure 18. The added presence of $\text{CH}_3\text{C}_2\text{H}$ as a photochemically active species in the N-C-H-O network will likely strengthen the photochemical shielding mechanism, making this an important future addition. Moreover, on Titan, $\text{CH}_3\text{C}_2\text{H}$ has been found at ten times higher abundances than CH_2CCH_2 (Lombardo et al., 2019), motivating the joint inclusion of both C_3H_4 isomers. Evidently, any upper limit on hydrocarbon complexity should include a quantification of the potential photochemical impact in the context of reducing atmospheres on rocky exoplanets.

Once reasonably complex hydrocarbons form, we know from Titan that an inevitable consequence is the formation of hydrocarbon hazes in such a reducing environment (e.g., Khare et al., 1984; Trainer et al., 2006; Tomasko et al., 2008; Lavvas et al., 2008; Hörst, 2017; Nixon, 2024). Absorption of UV photons in Titan's atmosphere is dominated by CH_4 at wavelengths <145 nm, by C_2H_2 and C_2H_4 until 180 nm, and by hazes beyond 180 nm (Vuitton et al., 2019), although the expected size, composition, and optical properties of hazes can vary significantly (e.g., He et al., 2018). We similarly expect potential shielding by hazes to affect the climate and chemistry of the reducing environment of Early Earth (e.g., Clarke & Ferris, 1997; Trainer et al., 2006; Domagal-Goldman et al., 2008). Examples include enhanced

Table 4

Key termolecular reactions in the pathways to feedstock molecules (particularly the hydrocarbons), comparing N-C-H-O and CRAHCN-O. We provide the rate coefficients A_0 , b_0 , $E_{a,0}$, A_∞ , b_∞ , and $E_{a,\infty}$ as well as k_{298} at 298 K and $[M]=2.5 \times 10^{19}$ molec cm^{-3} . Note that agreement in k_{298} does not necessarily imply agreement at the lower temperatures relevant to much of the simulated atmosphere (see 1).

R	Reaction (+ M)	$[A_0, b_0, E_{a,0}]$; $[A_\infty, b_\infty, E_{a,\infty}]$		k_{298} ($\text{cm}^6 \text{s}^{-1}$)	
		CRAHCN-O	N-C-H-O	CRAHCN-O	N-C-H-O
R25	$\text{CH}_3 + \text{CH}_3 \longrightarrow \text{C}_2\text{H}_6$	[1.7e-26, 0, 0]; [6e-11, 0, 0]	[3.5e-07, -7, 1390]; [1.58e-09, -0.54, 68.6]	6.00e-11	5.78e-11
R33	$\text{CH}_2 + \text{C}_2\text{H}_2 \longrightarrow \text{C}_3\text{H}_4$	[N/A]; [N/A]	[3.09e-15, -3.21, 162]; [1.07e-16, 1.48, -831]	N/A	7.99e-12
R36	$\text{C}_4\text{H}_2 + \text{H} \longrightarrow \text{C}_4\text{H}_3$	[N/A]; [N/A]	[6.16e-03, -8.9, 1261]; [7.08e-14, 1.16, 882]	N/A	2.72e-12
R44	$\text{C}_2\text{H}_2 + \text{C}_4\text{H}_3 \longrightarrow \text{C}_6\text{H}_5$	[N/A]; [N/A]	[3e-23, -1, 0]; [1.16e-09, -0.86, 3210]	N/A	1.81e-16
R45	$\text{C}_6\text{H}_5 + \text{H} \longrightarrow \text{C}_6\text{H}_6$	[N/A]; [N/A]	[1.3e-29, 0, 380]; [6.94e-11, 0.15, 0]	N/A	5.83e-11
R23	$\text{C}_3\text{H}_2 + \text{H} \longrightarrow \text{C}_3\text{H}_3$	[N/A]; [N/A]	[4e-19, -3, 600]; [1.26E-10, 0.102, -43.7]	N/A	5.06e-10
R46	$\text{C}_3\text{H}_3 + \text{H} \longrightarrow \text{C}_3\text{H}_4$	[N/A]; [N/A]	[1.6e-20, -3.3, 0]; [3.33e-11, 0.21, -87.1]	N/A	1.40e-10
R50	$\text{CH}_4 + \text{CH}_2(^1A_1) \longrightarrow \text{C}_2\text{H}_6$	[7.2e-24, 0, 0]; [7.1e-11, 0, 0]	[N/A]; [N/A]	7.10e-11	N/A

R25: Baulch et al. (1992); Macpherson et al. (1983); Baulch et al. (1994), R33: Laufer et al. (1983); Polino et al. (2013), R36: Klippenstein & Miller (2005), R44: estimated from Moses et al. (2016); Westmoreland et al. (1989), R45: estimated from Harding et al. (2005), R23: Harding et al. (2007); Moses et al. (2016), R46: Harding et al. (2007); Moses et al. (2011), R50: Tsang & Hampson (1986); Pearce et al. (2019).

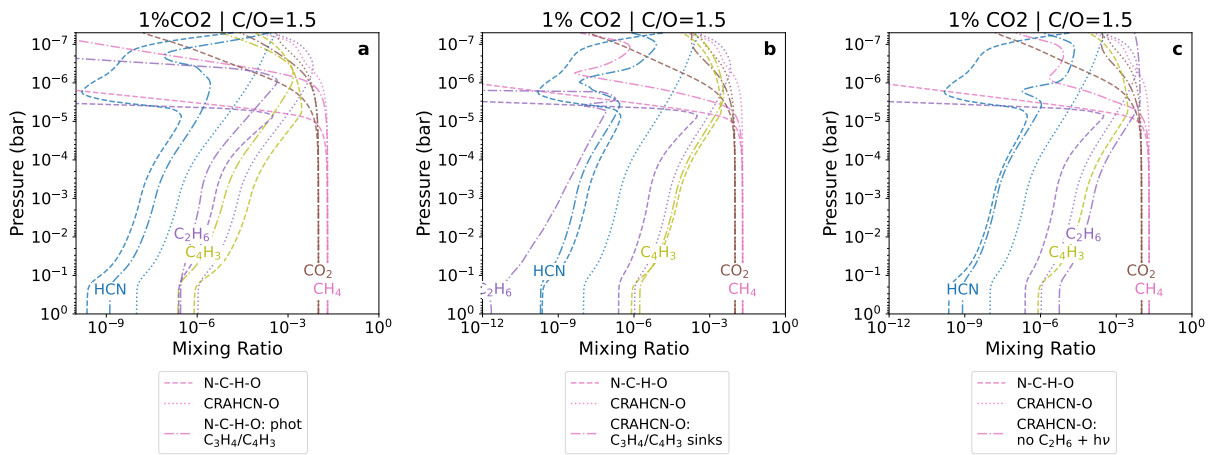


Figure 18: Three avenues for reconciliation: (a) photochemically active C_3H_4 and C_4H_3 in the N-C-H-O network provide shielding effects, whereas (b) artificial destruction of C_2H_6 into not photochemically active C_3H_4 and C_4H_3 in CRAHCN-O and (c) no photodissociation of C_2H_6 in CRAHCN-O weaken the shielding effects.

NH_3 abundances due to hydrocarbon haze shielding that potentially explain the Faint Young Sun paradox (Sagan & Chyba, 1997; Pavlov et al., 2001; Wolf & Toon, 2010). Arney et al. (2016) use a coupled 1D climate-chemistry model to explore the haze formation process and its climate impacts, showing that hazes can cool the surface of the Early Earth and provide UV shielding effects. However, due to self-shielding by hazes, catastrophic cooling of the planet is not predicted. For M-stars, the cooling effects are reduced, but a significant haze layer forms in the upper atmosphere with UV shielding effects (Arney et al., 2017). As both previous studies predict haze formation for atmospheric temperatures similar to ours (Arney et al., 2016, 2017), we also expect haze production. However, haze formation here is parameterised based on gaseous hydrocarbon abundances, following approaches used for Titan (Lavvas et al., 2008) and Titan-like exoplanets (Lora et al., 2018; Adams et al., 2022). 3D climate simulations using a prescribed haze layer confirm the UV shielding effects as well as the strong decrease of the surface temperature for Early Earth and a tidally locked exoplanet (Mak et al., 2023, 2024), along with potential circulation regime changes for the latter.

Lora et al. (2018) also parameterise haze production rates as combined rates of the reactions forming hydrocarbons with 10 or more C atoms, following Lavvas et al. (2008) for Titan. For Titan-like exoplanets around M-dwarfs, significant haze formation rates are predicted between 10^{-3} and 10^{-10} bar. For these pressures, hazes might actually provide shielding. However, further work should explore haze formation, their persistence (compared to advection, settling, rainout), and their potential shielding effects in (rocky) exoplanet settings. The recent detections of CH_4 mixing ratios at percent levels in sub-Neptune atmospheres (e.g., Madhusudhan et al., 2023; Schmidt et al., 2025),

along with potential hints of hydrocarbons such as C_3H_4 (Welbanks et al., 2025; Pica-Ciamarra et al., 2025), highlights the importance of understanding hydrocarbon chemistry in the appropriate environmental settings and warrants further studies in warmer and hydrogen-rich atmospheric settings (e.g., Adams et al., 2022; Cooke & Madhusudhan, 2024).

4.2. Considerations for prebiotic chemical processes

In the context of rocky planets, Rimmer & Rugheimer (2019) use the ARGO/STAND2020 photochemical kinetics model to investigate how HCN formation depends on C/O ratio and the particular atmospheric composition, reporting HCN mixing ratios varying between 1–1000 ppm for $0.5 < C/O \leq 1.5$. Our distribution of mixing ratios for $C/O > 0.5$ in Figure 5 with CRAHCN-O similarly ranges between 0.1–1000 ppm, depending on both the CO_2 background case and the C/O ratio. N-C-H-O predictions remain at the lower end of this range (0.05–3 ppm) and, for a given C/O, are relatively insensitive to the availability of CH_4 at the order of hundreds of ppm, per cent, or tens of per cent. A comparison with ARGO/STAND2020 in Appendix A confirms that HCN abundances in ARGO are similar to those with CRAHCN-O and sometimes even exceed them. The photochemical shielding effects are less pronounced, although this might also be due to ion-neutral chemistry in the upper atmosphere with ARGO (Rimmer & Helling, 2016). The impact of stellar radiation on HCN photochemistry is also summarised by Rimmer & Rugheimer (2019): 50–100 nm and 100–200 nm photons drive HCN production (N_2 photolysis) and destruction (H_2O photolysis), respectively. In our study, N_2 photolysis is relatively unaffected by C_2H_6 shielding in CRAHCN-O, but H_2O and CO_2 shielding limit the oxidising capacity of the upper atmosphere and thus allow HCN to form more abundantly. In a separate study, we further explore how the physical parameter space of rocky exoplanets affects atmospheric synthesis of HCN and subsequent rainout (Friss et al., 2025). Using the N-C-H-O network, we confirm trends with C/O and show how semi-major axes and host star type affect prebiotic synthesis. Once HCN accumulates in a shallow pond at the surface, a model of aqueous chemistry can simulate the formation of more complex prebiotic molecules (e.g., Pearce et al., 2022b). Since the prebiotic complexity achieved is dictated by UV irradiation (Ranjan & Sasselov, 2016), photochemical shielding is an important consideration. Ranjan & Sasselov (2016) demonstrated photochemical shielding of feedstock molecules like CH_4 and HCN by atmospheric CO_2 . Evidently, various hydrocarbons can potentially provide similar shielding mechanisms (Yoshida et al., 2024, and this work). Understanding such shielding mechanisms in the coupled physical and (photo)chemical environments is crucial to predicting the potential for prebiotic synthesis.

Nevertheless, planetary atmospheres are inherently 3D, with several physical and chemical implications for the distribution of feedstock molecules that are not captured in 1D. This study and the related work presented in Friss et al. (2025) pave the way for an implementation of prebiotic chemistry in a 3D climate-chemistry model, complex models that are currently limited by the number of reactions they can feasibly simulate. By identifying the key pathways in the specific environmental setting, as in Section 3.3, we demonstrate which reactions are crucial for a given chemical compound. Furthermore, the approximation of these pathways by net reactions such as shown for hydrocarbons in Section 3.3.3, allows for a considerable reduction of the complexity of a chemical network (Tsai et al., 2022; Lee et al., 2023). The gas-phase chemistry of these hydrocarbons can be used to construct a chemically consistent haze formation mechanism (e.g., Arney et al., 2016) to further explore the 3D effects of radiatively active hazes (Mak et al., 2023, 2024). 3D models accurately capture the effects of spatial and temporal variations in stellar radiation and climate from orbital configurations (Linsenmeier et al., 2015; Turbet et al., 2016; Boutle et al., 2017; Del Genio et al., 2019), associated chemical and wet-dry cycles (Braam et al., 2025), and the effects of energetic events such as stellar flares (Chen et al., 2021; Ridgway et al., 2023a) and lightning (Braam et al., 2022; Sergeev et al., 2025), all impacting the potential production of feedstock molecules. We note that results on feedstock molecules as well as hydrocarbon shielding might change when accounting for stellar evolution (e.g., Claire et al., 2012). Future work will be directed to simulations of prebiotic chemistry that account for the evolution of stellar UV emission from M stars (e.g., Shkolnik & Barman, 2014; Peacock et al., 2020).

4.3. Chemical network recommendations

In Section 3.3, we present the key pathways to important feedstock molecules (HCN, HC_3N , H_2CO , and hydrocarbons), comparing two independently constructed chemical networks. Key bimolecular reactions are listed and compared in Table 3, along with a recommendation on using the rate coefficient from CRAHCN-O (C), N-C-H-O (N), or further rate coefficient determination (M). The recommendations are based on a comparison to the reported rate coefficient measurements. For the key termolecular reactions in Table 4, Reaction R25 is well-constrained by multiple independent measurements, whereas the other hydrocarbon reactions in Table 4 are typically based on a single experimental measurement, thus justifying further rate coefficient determinations. As noted in Section 4.1, the pathways

and key reactions can be used to reconcile chemical network differences. In what follows, we discuss recommended network improvements, focusing on feedstocks and hydrocarbons, as informed by the key pathways, shielding effects, and rate coefficient comparisons of this work.

A fundamental difference in HCN formation is its dependence on HNCO through Reactions R3–R7, present in the N-C-H-O but not in the CRAHCN-O network. The role of HNCO in hot Jupiter atmospheres is also discussed by Moses et al. (2011) and Tsai et al. (2021). The HNCO rate coefficients in Tables 3 are valid for temperatures exceeding the atmospheric conditions in this work: 1830–2400 K for R3, 500–2500 K for R5 and R7, and 300–3300 K for R4. This extrapolation to low temperatures also applies to many of the rate coefficients normally used for Titan (e.g., Lavvas et al., 2008). Whilst the ranges for R7, R5, and R4 may be acceptable, our simulations are far from the valid temperature range of R3, which also lacks temperature dependence in its rate coefficient in N-C-H-O (as $A=0$). Therefore, an inclusion of HCN production through the HNCO reactions requires a low-temperature constraint of the rate coefficients for Reactions R3–R7, in particular R3. The coefficients for the other important HCN pathway, Reaction R2, agree at 298 K (Table 3), but do decrease for lower temperatures in N-C-H-O. However, as the N-C-H-O rate coefficient is an estimate based on the $N + CH_3 \longrightarrow HCN + H_2$ coefficients from Marston et al. (1989), we recommend additional measurements. CRAHCN-O has a fast pathway to HCN with H_2CO as an intermediate species via Reaction R19. Since the rate coefficient of Reaction R19 in CRAHCN-O originates from a single experimental determination, we recommend additional measurements. Since HCN and HNC are one of the two known isomer pairs in Titan's atmosphere (Moreno et al., 2011), HNC chemistry should be added to the N-C-H-O network.

HC_3N formation is relatively fast in N-C-H-O, due to its dependence on hydrocarbons such as C_2H (R28), C_2H_2 (R27), and C_3H_3 (R24). However, the rate coefficients for Reactions R28 and R24 need further validation. In CRAHCN-O, HC_3N formation is much slower due to low hydrocarbon abundances and the missing Reaction R24. Since HC_3N plays an important role in several steps of prebiotic synthesis (Powner et al., 2007, 2009; Patel et al., 2015), we recommend the inclusion of additional HC_3N pathways in CRAHCN-O, thus also motivating a more comprehensive treatment of C_2H_2 and C_3H_3 . The measured abundances of HC_3N on Titan can be used to validate the pathways (Thelen et al., 2019).

The higher H_2CO abundances in CRAHCN-O follow from fast HCO production via Reaction R17, which quickly self-reacts (R18) to form H_2CO in CRAHCN-O. We note that for Reaction R17, Pearce et al. (2020a) present the rate coefficients for the forward reaction $HCO + H \longrightarrow CO + H + H$, which is reversed in VULCAN using the equilibrium constant (Tsai et al., 2017). As such, additional constraints on the rate coefficients of the reverse reaction are valuable. At high pressures for N-C-H-O, H_2CO production through Reaction 32 follows rate coefficients in the database presented by Tsang & Hampson (1986), resulting in enhanced H_2CO abundances compared to CRAHCN-O. However, the single experimental determination for Reaction 32 motivates additional measurements.

The treatment of hydrocarbons in N-C-H-O generally focuses on C2 hydrocarbons. Higher-order hydrocarbons were included in a simplified mechanism to form benzene as a haze precursor (Tsai et al., 2021). Purposefully, this includes only the main formation pathways to benzene to limit the network size, although this is also due to limitations of the available kinetics data (Venot et al., 2015). Among the key bimolecular reactions in the hydrocarbon pathways, Reactions R22, R35, R41, and R47 are relatively well-constrained by multiple measurements and/or reviews across the relevant temperature range. The destruction of C_3H_4 via Reaction R43 has several measured sets of rate coefficients, but no dedicated review, and is generally reported for temperatures exceeding 600 K. The termolecular reactions in Table 4 are usually based on a single measurement (Reactions R33 and R36) or estimated from other reactions (Reaction R44, R45, R23, R46, R50), motivating additional rate coefficient determination. Due to the dominance of C_2H_6 formation in CRAHCN-O by Reactions R48 and R49, we suggest further determination of the reverse reactions. Since C3 and C4 molecules are likely also photochemically active, we recommend including their cross sections in N-C-H-O (like for C_3H_4 in Section 4.1). Since allene and propyne are the other known isomer pair in Titan's atmosphere (Lombardo et al., 2019), the networks have to be expanded with an isomeric treatment (Hébrard et al., 2013; Vuitton et al., 2019). Ultimately, the hydrocarbon partitioning should be determined by a more complete expansion of hydrocarbon interactions with other species and, eventually, by parameterising haze formation (e.g. Lavvas et al., 2008; Lora et al., 2018; Adams et al., 2022). Based on this, any simplified hydrocarbon scheme should include an assessment of the photochemical effects.

An alternative approach to quantify network sensitivity and efficient network reduction is to apply a genetic algorithm such as DARWEN (Lira-Barría et al., 2024). In our VULCAN configurations, the chemistry is mainly driven by the photodissociation reactions. As we know from Titan, energetic particles and cosmic rays also drive a plethora of photochemical processes and the comparison to ARGO hints at ion-neutral effects (see Section A). Future work

can build upon the wealth of knowledge in models of Titan photochemistry (Loison et al., 2015; Dobrijevic et al., 2016; Vuitton et al., 2019) and consider the effect of the upper boundary, considering photodissociation, electron impacts, and ion-neutral interactions. Nevertheless, the model predictions for any chemical networks will have to be tested against lab experiments, quantum chemical calculations, and observations of planetary environments. For the networks considered here, N-C-H-O was benchmarked against Earth, Jupiter, and previous models of hot Jupiters (Tsai et al., 2021). For Earth, the network reproduces the main photochemical cycles and also validates VULCAN's inclusion of boundary conditions and H₂O condensation. Jupiter observations are used to validate the hydrocarbon predictions, providing good agreement for CH₄ and C₂ hydrocarbons. However, Tsai et al. (2021) note uncertainties in the rate constants for hydrocarbon reactions at temperatures below 200 K and in the higher-order hydrocarbons, notably C₄H₂ and C₆H₆. The hot Jupiter results are compared to earlier model results by Moses et al. (2011) and Venot et al. (2012), validating the effects of photochemistry and vertical mixing. CRAHCN-O was benchmarked against HCN on Titan (Pearce et al., 2020a), but does not reproduce other small prebiotic feedstocks or hydrocarbons like the Titan photochemical models commonly do (Loison et al., 2015; Dobrijevic et al., 2016; Willacy et al., 2016; Vuitton et al., 2019). Pearce et al. (2020b) show how the CRAHCN-O predictions for the lower atmosphere of Titan fall in the middle of the Cassini measurements and also match the in-situ upper atmosphere Cassini INMS data point. However, like most photochemical models, it fails to reproduce the observed variability in upper-atmospheric HCN profiles from Cassini and ground-based measurements (see also Lellouch et al., 2019; Thelen et al., 2022). Accurately modelling this variability may require higher-dimensional photochemical models to account for seasonal and dynamical effects (De La Haye et al., 2008; Dobrijevic et al., 2021). The simulated network differences illustrate the environmental dependence: benchmarking in one scenario does not inherently imply agreement in another. Moreover, beyond differences in chemical networks, the environmental conditions ultimately determine the chemical pathways. Future plans include a Titan configuration in VULCAN, likely based on the CRAHCN-O chemical network. In turn, this should also advance further modelling of reducing atmospheric conditions on exoplanets.

Investigating prebiotic chemistry in exoplanet atmospheres ultimately feeds into finding the likelihood of certain planetary conditions leading to a specific set of feedstock molecules (Sutherland, 2017; Benner et al., 2019; Rimmer, 2023; White & Rimmer, 2025). The dependence on boundary conditions and the likelihood of specific reactions occurring in sequence necessitate the use of photochemical kinetics models with associated chemical networks. However, a chemical network is more an expression of our knowledge of the system than a complete representation of reality (White & Rimmer, 2025), emphasising the importance of network comparisons for distinct environments. Associated pathway analyses, such as in Section 3.3, can quantify the likelihood of specific reactions occurring in sequence and help determine whether a network is comprehensive enough to represent the prebiotic scenario of interest in the environmental conditions. Understanding net reactions and chemical mechanisms allows for network comparison and guides explorations of the chemical processes in more complex atmospheric models (Tsai et al., 2022; Lee et al., 2023). By determining the most important reactions per network, we identify those that may require further experimental rate constant determination and the conditions under which these measurements would be most useful. For example, our results emphasise the crucial role of hydrocarbon reactions in predicting the production of feedstock molecules for M-star radiation. Both the net and important reactions provide a base for connecting global environmental properties to a given prebiotic scenario and, specifically for exoplanets, quantify the so-called Abiogenesis Zone based on known exoplanet properties such as stellar irradiation and orbital distance (Rimmer et al., 2018; Rimmer, 2023). Ultimately, this knowledge of chemical kinetics will help us understand whether the emergence of life is more or less likely in a given planetary environment.

4.4. Conclusions

In summary, we present the implementation of the CRAHCN-O chemical network into the VULCAN 1D photochemical kinetics code (Tsai et al., 2021). CRAHCN-O was specifically constructed to accurately simulate HCN and H₂CO, simple hydrocarbons, NH₃, and other small organic species in various atmospheric compositions at temperatures of 50–400 K (Pearce et al., 2020a). We test the production of prebiotic feedstock molecules driven by irradiation from M-star hosts and compare the results to predictions by the N-C-H-O network in VULCAN. Various initial atmospheric compositions for the simulations cover C/O ratios of 0.5–1.5 and C/N ratios between 2×10^{-4} – 2×10^{-1} . We find agreement between the vertical distributions of mixing ratios in the absence of CH₄ for C/O=0.5, but diverging distributions when CH₄ is introduced for C/O>0.5. Inter-network differences in hydrocarbon complexity and subsequent photochemical shielding drive the diverging mixing ratio profiles. The most complex hydrocarbon in CRAHCN-O is C₂H₆, which accumulates in the upper atmosphere. Importantly, C₂H₆ has known photochemical

shielding effects, and its high abundance shields CH_4 and CO_2 from photodissociation, allowing their existence at lower pressures and reducing the production of reactive oxygen species that destroy HCN and H_2CO . The N-C-H-O network simulates more complex hydrocarbons, including C_4H_3 , C_3H_4 , and C_6H_6 , that instead accumulate in the upper atmosphere. However, they are not photochemically active and are thus unable to provide the same photochemical shielding. Other feedstock molecules, such as HC_3N and C_2H_2 , form much more efficiently in N-C-H-O. The shielding mechanism and weak formation of HC_3N and C_2H_2 persist across M-star types. We determine the key pathways to feedstock molecules in both networks and derive formation mechanisms to explain the distinct hydrocarbon profiles and shielding effects. The results demonstrate the crucial role of chemical kinetics in understanding prebiotic chemistry in exoplanet atmospheres, including important considerations for constructing chemical networks. In a related paper, we explore how the atmospheric feedstock molecules are transferred to the planetary surface (Friss et al., 2025), where aqueous chemistry can drive further complexity. We identify several paths forward: to expand the hydrocarbon complexity and their photochemical properties, to test the effect of hazes in the shielding scenario, and to use the identified pathways and net reactions to explore prebiotic chemistry in 3D climate-chemistry models. Lastly, we discuss recommended network improvements, based on the network comparison and known mechanisms of importance for Titan's atmospheric chemistry.

Acknowledgements

MB thanks Arturo Lira-Barria, Jeremy Harvey, and Susanne Wampfler for helpful discussions about rate coefficient uncertainties, chemical mechanisms, and previous astrochemical network analyses. We thank Ben K. D. Pearce and the anonymous reviewer whose comments helped to significantly improve the manuscript. MB appreciates support from a CSH Fellowship. Part of this work has been carried out within the framework of the NCCR PlanetS supported by the Swiss National Science Foundation under grants 51NF40_182901 and 51NF40_205606. EG acknowledges a Summer Internship supported by the Centre for Exoplanet Science, University of Edinburgh. GF acknowledges his studentship by the Science and Technology Facilities Council (project reference: 2902875). PIP acknowledges funding from the STFC consolidator grant ST/V000594/1. MB and PIP were part of the CHAMELEON MC ITN EJD, which received funding from the European Union's Horizon 2020 research and innovation program under the Marie Skłodowska-Curie grant agreement No. 860470.

A. ARGO/STAND2020 Comparison

To further expand our comparison of chemical networks in relatively unexplored environments, we conduct an additional set of six photochemical simulations using ARGO – a Lagrangian code that solves the photochemistry-transport equation – and the extensive STAND2020 chemical network that includes over 6000 reactions for 480 species (Rimmer & Helling, 2016; Rimmer et al., 2021). Our simulation sets include the 1% and 10% CO_2 scenarios for C/O ratios of 0.5, 1.0, and 1.5. Except for the photochemical kinetics solver and the chemical network, the initialisation (Table 1) and boundary conditions (Figure 1) remain the same. For the ARGO simulations in this comparison, the surface mixing ratio of H_2O is not fixed at 0.00894 but instead initialised as 1 ppm on all vertical levels.

Figure 19 shows the distribution of initialisation species CH_4 , CO_2 , and H_2O after each of the three models (VULCAN/CRAHCN-O, VULCAN/N-C-H-O, ARGO/STAND2021) has reached steady state. For C/O=0.5, we again see good agreement between models for CO_2 and H_2O . Destruction of CO_2 in ARGO is stronger for $P < 10^{-6}$ bar, most likely as a consequence of the inclusion of ionisation and resulting ion-neutral reactions in the network. Ionisation and ion-neutral reactions normally drive chemical processes at much lower pressures (to as low as $\sim 10^{-12}$ bar). Due to our upper boundary at 5×10^{-8} bar, the ionisation processes are instead simulated at higher pressures, affecting the predicted vertical profiles in the photochemical region as seen for the CO_2 destruction. Moving to higher C/O ratios, we see again that CO_2 destruction is more efficient than in both networks in VULCAN. H_2O is in good agreement with N-C-H-O. Notably, Figures 19c–f, we see that CH_4 is stable to lower pressures using ARGO compared to N-C-H-O, potentially pointing to differences in hydrocarbons and photochemical shielding. In no simulation is CH_4 shielding as efficient as the predictions by CRAHCN-O.

We separately plot the feedstock molecules and a selection of hydrocarbons (C_2H_2 , C_2H_6 , C_3H_4 , C_4H_3) for C/O=1.0 and 1.5 in Figure 20. Panels a, b, e, and f correspond to the 1% CO_2 and panels c, d, g, and h to the 10% CO_2 cases, respectively. We omit the results for C/O=0.5 here because of the negligible feedstock and hydrocarbon abundances (like in Figure 3a and b). Especially for the feedstock molecules (Figures 20a,e for 1% CO_2

and Figures 20c,g for 10% CO₂), the ARGO comparison adds further ambiguity. Whilst HCN in ARGO peaks at abundances similar to and occasionally higher than CRAHCN-O (Figure 20e), the HC₃N dotted agrees more with the N-C-H-O predictions. H₂CO abundances are considerably lower than either of the two networks in VULCAN, hinting at slower production or additional destruction pathways in ARGO.

In terms of hydrocarbons, ARGO predicts lower abundances for C₂H₂ than N-C-H-O in a spiky profile (Figures 20b, d, f) but reasonably similar abundances for the C/O=1.5 case at 10% CO₂ (Figure 20h). C₂H₆ abundances with ARGO are also two to three orders of magnitude lower than N-C-H-O at C/O=1.0 (Figure 20b, d). The C₂H₆ profile in ARGO also goes down to lower pressures, and its shielding effects lift HCN profiles (Figure 20a, b, c, g) and the regions subject to CH₄ photochemistry (Figure 19) to lower pressures. In Figure 20h, we see that N-C-H-O and ARGO also predict comparable C₂H₆ profiles. C₃H₄ and C₄H₃ are included in this comparison as sinks for lower-order hydrocarbons that are notably not photochemically active in VULCAN. Peak abundances of C₃H₄ in ARGO are similar to N-C-H-O, but these abundance peaks go up to the top boundary of the atmosphere. Also, like N-C-H-O, C₃H₄ is not treated as photochemically active in ARGO. C₄H₃ is predicted at low (<10⁻¹⁰) mixing ratios in ARGO. Therefore, in ARGO, we also suspect hydrocarbon accumulation in C₃H₄ without providing a photochemical shielding mechanism.

The comparison highlights some important discussion points. First, networks that have been benchmarked for one set of environmental conditions can predict differences for another set of environmental conditions. Second, the effect of neutral-ion chemistry in ARGO illustrates the importance of the correct upper boundary given the processes considered, e.g. to as low as ~10⁻¹² bar when neutral-ion chemistry is included. Third, hydrocarbon complexity in a chemical network and its potential shielding effects are key to predicting the production of feedstock molecules. Finally, as different panels in Figures 3, 19, and 20 demonstrate, exact abundance differences due to chemical networks are also sensitive to the chosen boundary and initial conditions.

CRedit authorship contribution statement

Marrick Braam: Conceptualisation, Methodology, Formal analysis, Investigation, Writing - Original Draft, Visualisation. **Ellery Gopaoco:** Conceptualisation, Methodology, Formal analysis, Investigation, Writing - Original Draft. **Shang-Min Tsai:** Methodology, Investigation, Formal analysis, Writing - Review & Editing. **Gergely Friss:** Methodology, Validation, Writing - Review & Editing. **Paul I. Palmer:** Conceptualisation, Methodology, Writing-Reviewing and Editing, Funding acquisition. **Paul B. Rimmer:** Methodology, Investigation, Writing-Reviewing and Editing. **Skyla B. White:** Conceptualisation, Writing - Review & Editing.

References

- Adams, D., Luo, Y., & Yung, Y. L. 2022, *Frontiers in Astronomy and Space Sciences*, 9. <https://www.frontiersin.org/articles/10.3389/fspas.2022.823227>
- Airapetian, V., Barnes, R., Cohen, O., et al. 2020, *International Journal of Astrobiology*, 19, 136
- Airapetian, V. S., Glocer, A., Gronoff, G., Hébrard, E., & Danchi, W. 2016, *Nature Geoscience*, 9, 452, doi: 10.1038/ngeo2719
- Anglada-Escudé, G., Amador, P. J., Barnes, J., et al. 2016, *nature*, 536, 437
- Archibald, A. T., O'Connor, F. M., Abraham, N. L., et al. 2020, *Geoscientific Model Development*, 13, 1223, doi: <https://doi.org/10.5194/gmd-13-1223-2020>
- Ardaseva, A., Rimmer, P. B., Waldmann, I., et al. 2017, *Monthly Notices of the Royal Astronomical Society*, 470, 187, doi: 10.1093/mnras/stx1012
- Arney, G., Domagal-Goldman, S. D., Meadows, V. S., et al. 2016, *Astrobiology*, 16, 873, doi: 10.1089/ast.2015.1422
- Arney, G. N., Meadows, V. S., Domagal-Goldman, S. D., et al. 2017, *The Astrophysical Journal*, 836, 49, doi: 10.3847/1538-4357/836/1/49
- Atkinson, R., Baulch, D. L., Cox, R. A., et al. 1997, *Journal of Physical and Chemical Reference Data*, 26, 521, doi: 10.1063/1.556011
- , 1989, *Journal of Physical and Chemical Reference Data*, 18, 881, doi: 10.1063/1.555832
- Bada, J. L. 2004, *Earth and Planetary Science Letters*, 226, 1, doi: 10.1016/j.epsl.2004.07.036
- , 2013, *Chemical Society Reviews*, 42, 2186, doi: 10.1039/c3cs35433d
- Bada, J. L., & Lazcano, A. 2002, *Science*, 296, 1982, doi: 10.1126/science.1069487
- Baeyens, R., Decin, L., Carone, L., et al. 2021, *Monthly Notices of the Royal Astronomical Society*, 505, 5603
- Balucani, N. 2009, *International Journal of Molecular Sciences*, 10, 2304, doi: 10.3390/ijms10052304
- Barnes, R. 2017, *Celestial mechanics and dynamical astronomy*, 129, 509
- Barth, P., Stüeken, E. E., Helling, C., Schwieterman, E. W., & Telling, J. 2024, *Astronomy & Astrophysics*, 686, A58, doi: 10.1051/0004-6361/202347286
- Bates, D. R., & Nicolet, M. 1950, *Journal of Geophysical Research (1896-1977)*, 55, 301, doi: 10.1029/JZ055i003p00301
- Baulch, D. L., Cobos, C. J., Cox, R. A., et al. 1992, *Journal of Physical and Chemical Reference Data*, 21, 411, doi: 10.1063/1.555908
- Baulch, D. L., Cobos, C. J., Cox, R. A., et al. 1994, *Journal of Physical and Chemical Reference Data*, 23, 847, doi: 10.1063/1.555953

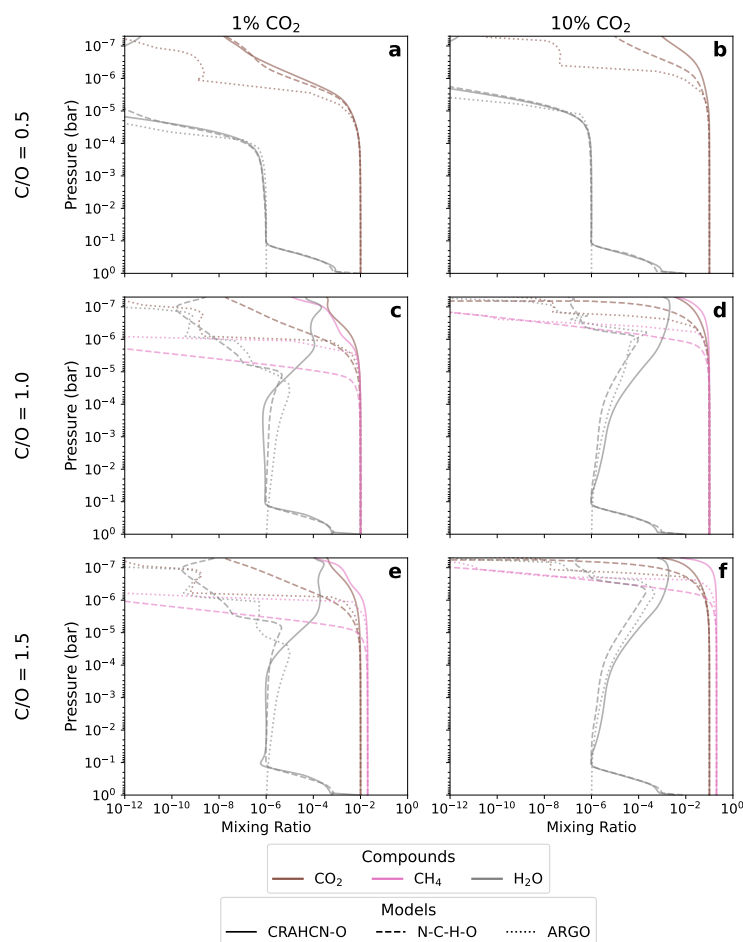


Figure 19: Grid comparing the chemical abundance profiles of initialisation species versus atmospheric pressure for the 1 % (left), and 10% (right) CO₂ cases to predictions made by ARGO/STAND2021 code. The horizontal rows correspond to C/O=0.5, 1.0, and 1.5, respectively, whereas solid lines correspond to the VULCAN/CRAHCN-O, dashed lines to the VULCAN/N-C-H-O, and dotted lines to ARGO/STAND2021 simulations.

- Benmahi, B., Cavalié, T., Fouchet, T., et al. 2022, *Astronomy & Astrophysics*, 666, A117, doi: 10.1051/0004-6361/202244200
- Benner, S. A., Kim, H.-J., & Biondi, E. 2019, *Life*, 9, 84, doi: 10.3390/life9040084
- Benner, S. A., Bell, E. A., Biondi, E., et al. 2020, *ChemSystemsChem*, 2, e1900035, doi: 10.1002/syst.201900035
- Berman, M. R., & Lin, M. C. 1983, *Chemical Physics*, 82, 435, doi: 10.1016/0301-0104(83)85248-3
- Boutle, I. A., Mayne, N. J., Drummond, B., et al. 2017, *Astronomy & Astrophysics*, 601, A120, doi: 10.1051/0004-6361/201630020
- Braam, M., Palmer, P. I., Decin, L., et al. 2025, *The Planetary Science Journal*, 6, 5, doi: 10.3847/PSJ/ad9565
- , 2022, *Monthly Notices of the Royal Astronomical Society*, 517, 2383, doi: 10.1093/mnras/stac2722
- Butlerow, A. 1861, *CR Acad. Sci*, 53, 145
- Carone, L., Keppens, R., Decin, L., & Henning, T. 2018, *Monthly Notices of the Royal Astronomical Society*, 473, 4672, doi: 10.1093/mnras/stx2732
- Catling, D. C., & Zahnle, K. J. 2020, *Science Advances*, 6, eaax1420, doi: 10.1126/sciadv.aax1420
- Chameides, W. L., & Walker, J. C. G. 1981, *Origins of life*, 11, 291, doi: 10.1007/BF00931483
- Chapman, S. 1930, *The London, Edinburgh, and Dublin Philosophical Magazine and Journal of Science*, 10, 369
- Chen, H., Wolf, E. T., Koppurapu, R., Domagal-Goldman, S., & Horton, D. E. 2018, *The Astrophysical Journal*, 868, L6, doi: 10.3847/2041-8213/aaedb2
- Chen, H., Zhan, Z., Youngblood, A., et al. 2021, *Nature Astronomy*, 5, 298, doi: 10.1038/s41550-020-01264-1
- Chyba, C., & Sagan, C. 1992, *Nature*, 355, 125, doi: 10.1038/355125a0
- Claire, M. W., Sheets, J., Cohen, M., et al. 2012, *The Astrophysical Journal*, 757, 95, doi: 10.1088/0004-637X/757/1/95
- Claringbold, A., Rimmer, P., Rugheimer, S., & Shorttle, O. 2023, *The Astronomical Journal*, 166, 39, doi: 10.3847/1538-3881/acdacc
- Clarke, D. W., & Ferris, J. P. 1997, *Origins of life and evolution of the biosphere*, 27, 225, doi: 10.1023/A:1006582416293

Hydrocarbon shielding and prebiotic chemistry in exoplanet atmospheres

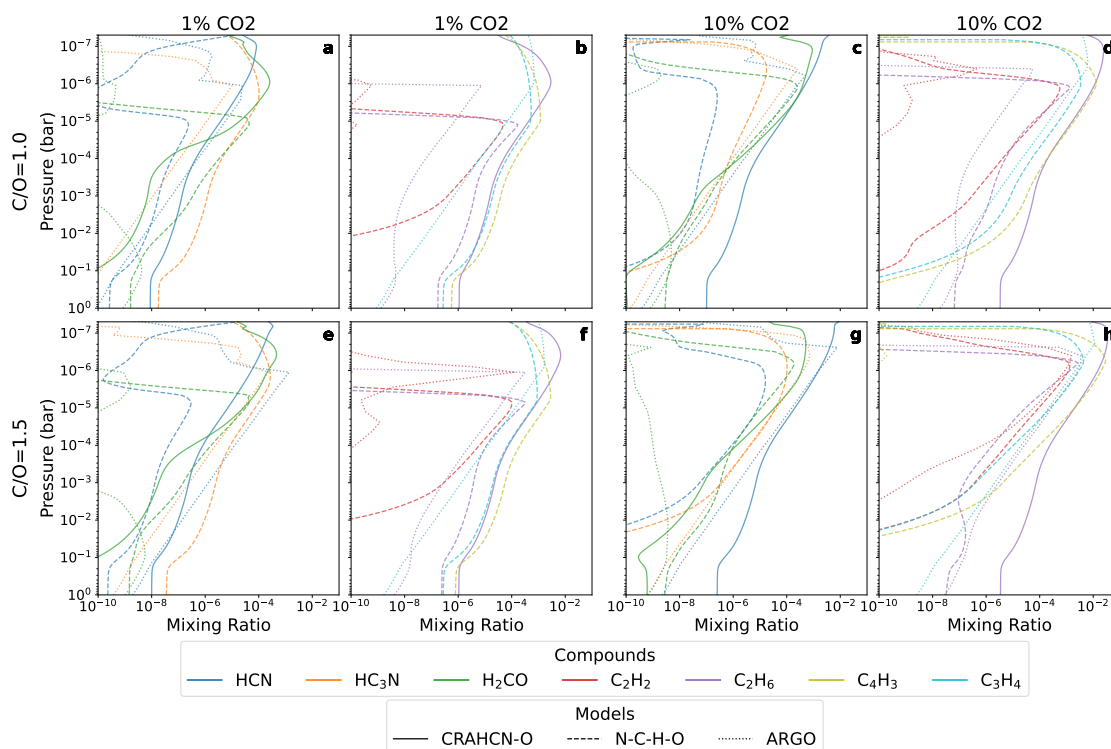


Figure 20: Grid comparing the vertical profiles of feedstock molecules for the 1 % (panels a, b, e, f), and 10% (panels c, d, g, h) CO_2 cases to predictions made by ARGO/STAND2021 photochemical kinetics code. For visual clarity, we separate HCN, HC_3N , and H_2CO in the left column for each scenario and C_2H_2 , C_2H_6 , C_3H_4 , and C_4H_3 in the right column. The horizontal rows correspond to $\text{C}/\text{O}=1.0$ and 1.5 , respectively, as $\text{C}/\text{O}=0.5$ barely produces these feedstock molecules (see Figure 3). Solid lines correspond to the VULCAN/CRAHCN-O, dashed lines to the VULCAN/N-C-H-O, and dotted lines to ARGO/STAND2021 simulations.

- Cleaves, H. J. 2008, *Precambrian Research*, 164, 111, doi: [10.1016/j.precamres.2008.04.002](https://doi.org/10.1016/j.precamres.2008.04.002)
- Cleaves, H. J., Chalmers, J. H., Lazcano, A., Miller, S. L., & Bada, J. L. 2008, *Origins of Life and Evolution of Biospheres*, 38, 105, doi: [10.1007/s11084-007-9120-3](https://doi.org/10.1007/s11084-007-9120-3)
- Cooke, G. J., & Madhusudhan, N. 2024, *The Astrophysical Journal*, 977, 209, doi: [10.3847/1538-4357/ad8cda](https://doi.org/10.3847/1538-4357/ad8cda)
- Cooke, G. J., Marsh, D. R., Walsh, C., Rugheimer, S., & Villanueva, G. L. 2023, *Monthly Notices of the Royal Astronomical Society*, 518, 206, doi: [10.1093/mnras/stac2604](https://doi.org/10.1093/mnras/stac2604)
- Crutzen, P. J. 1970, *Quarterly Journal of the Royal Meteorological Society*, 96, 320, doi: <https://doi.org/10.1002/qj.49709640815>
- Damer, B., & Deamer, D. 2020, *Astrobiology*, 20, 429, doi: [10.1089/ast.2019.2045](https://doi.org/10.1089/ast.2019.2045)
- Davidson, D., & Hanson, R. 1991, *Symposium (International) on Combustion*, 23, 267, doi: [https://doi.org/10.1016/S0082-0784\(06\)80269-9](https://doi.org/10.1016/S0082-0784(06)80269-9)
- Davis, S. G., Law, C. K., & Wang, H. 1999, *The Journal of Physical Chemistry A*, 103, 5889
- De La Haye, V., Waite, J. H., Cravens, T. E., Robertson, I. P., & Lebonnois, S. 2008, *Icarus*, 197, 110, doi: [10.1016/j.icarus.2008.03.022](https://doi.org/10.1016/j.icarus.2008.03.022)
- De Luca, P., Braam, M., Komacek, T. D., & Hochman, A. 2024, *Monthly Notices of the Royal Astronomical Society*, 531, 1471
- Dean, A. M., & Bozzelli, J. W. 2000, in *Gas-Phase Combustion Chemistry*, ed. W. C. Gardiner (New York, NY: Springer), 125–341, doi: [10.1007/978-1-4612-1310-9_2](https://doi.org/10.1007/978-1-4612-1310-9_2)
- Del Genio, A. D., Way, M. J., Amundsen, D. S., et al. 2019, *Astrobiology*, 19, 99, doi: [10.1089/ast.2017.1760](https://doi.org/10.1089/ast.2017.1760)
- Demore, W., Sander, S., Golden, D., et al. 1997, JPL Publication, 90
- Demore, W. B., Sander, S. P., Golden, D. M., et al. 1994, *Chemical kinetics and photochemical data for use in stratospheric modeling: Evaluation number 11*, Tech. rep., California Institute of Technology (CalTech), Pasadena, CA (United States). Jet Propulsion Lab. (JPL). <https://www.osti.gov/biblio/102024>
- Dijkstra, E. W. 1959, *Numerische Mathematik*, 1, 269, doi: [10.1007/BF01386390](https://doi.org/10.1007/BF01386390)
- Dobrijevic, M., Loison, J. C., Hickson, K. M., & Gronoff, G. 2016, *Icarus*, 268, 313, doi: [10.1016/j.icarus.2015.12.045](https://doi.org/10.1016/j.icarus.2015.12.045)
- Dobrijevic, M., Loison, J. C., Hue, V., & Cavalié, T. 2021, *Icarus*, 364, 114477, doi: [10.1016/j.icarus.2021.114477](https://doi.org/10.1016/j.icarus.2021.114477)
- Domagal-Goldman, S. D., Kasting, J. F., Johnston, D. T., & Farquhar, J. 2008, *Earth and Planetary Science Letters*, 269, 29, doi: [10.1016/j.epsl.2008.01.040](https://doi.org/10.1016/j.epsl.2008.01.040)

- Eiteneer, B., & Frenklach, M. 2003, *International Journal of Chemical Kinetics*, 35, 391
- Fegley, B., & Lodders, K. 1994, *Icarus*, 110, 117, doi: 10.1006/icar.1994.1111
- Ferris, J. P., & Orgel, L. 1966, *Journal of the American Chemical Society*, 88, 1074
- Fisher, T., Janin, E., & Walker, S. I. 2025, *The Planetary Science Journal*, 6, 116, doi: 10.3847/PSJ/adcc27
- France, K., Loyd, R. P., Youngblood, A., et al. 2016, *The Astrophysical Journal*, 820, 89
- Friss, G., Palmer, P., Braam, M., & Rice, K. 2025, Submitted
- Gannon, K. L., Glowacki, D. R., Blitz, M. A., et al. 2007, *The Journal of Physical Chemistry A*, 111, 6679, doi: 10.1021/jp0689520
- Garraffo, C., Drake, J. J., & Cohen, O. 2016, *The Astrophysical Journal Letters*, 833, L4
- Godolt, M., Grenfell, J., Hamann-Reinus, A., et al. 2015, *Planetary and Space Science*, 111, 62
- Goldreich, P., & Peale, S. 1966, *Astronomical Journal*, Vol. 71, p. 425 (1966), 71, 425
- Guadagnini, R., Schatz, G. C., & Walch, S. P. 1998, *The Journal of Physical Chemistry A*, 102, 5857
- Haldane, J. B. S. 1929, *Rationalist Annual*, 148, 3
- Hanel, R., Conrath, B., Flasar, F. M., et al. 1981, *Science*, 212, 192, doi: 10.1126/science.212.4491.192
- Haqq-Misra, J., Wolf, E. T., Joshi, M., Zhang, X., & Koppapu, R. K. 2018, *The Astrophysical Journal*, 852, 67, doi: 10.3847/1538-4357/aa9f1f
- Harding, L. B., Georgievskii, Y., & Klippenstein, S. J. 2005, *The Journal of Physical Chemistry A*, 109, 4646
- Harding, L. B., Klippenstein, S. J., & Georgievskii, Y. 2007, *The Journal of Physical Chemistry A*, 111, 3789
- Haynes, B. S., Iverach, D., & Kirov, N. Y. 1975, *Symposium (International) on Combustion*, 15, 1103, doi: 10.1016/S0082-0784(75)80375-4
- He, C., Hörst, S. M., Lewis, N. K., et al. 2018, *The Astronomical Journal*, 156, 38, doi: 10.3847/1538-3881/aac883
- Heng, K., Lyons, J. R., & Tsai, S.-M. 2016, *The Astrophysical Journal*, 816, 96, doi: 10.3847/0004-637X/816/2/96
- Hoobler, R. J., & Leone, S. R. 1997, *Journal of Geophysical Research*, 102, doi: 10.1029/97JE02526
- Hébrard, E., Dobrijevic, M., Bénilan, Y., & Raulin, F. 2007, *Planetary and Space Science*, 55, 1470, doi: 10.1016/j.pss.2007.04.006
- Hébrard, E., Dobrijevic, M., Loison, J. C., Bergeat, A., & Hickson, K. M. 2012, *Astronomy & Astrophysics*, 541, A21, doi: 10.1051/0004-6361/201218837
- Hébrard, E., Dobrijevic, M., Loison, J. C., et al. 2013, *Astronomy & Astrophysics*, 552, A132, doi: 10.1051/0004-6361/201220686
- Hörst, S., Yelle, R., Buch, A., et al. 2012, *Astrobiology*, 12, 809, doi: 10.1089/ast.2011.0623
- Hörst, S. M. 2017, *Journal of Geophysical Research: Planets*, 122, 432, doi: 10.1002/2016JE005240
- Jacob, D. J. 2000, *Atmospheric Environment*, 34, 2131, doi: 10.1016/S1352-2310(99)00462-8
- Joshi, M. M., Haberle, R. M., & Reynolds, R. T. 1997, *Icarus*, 129, 450, doi: 10.1006/icar.1997.5793
- Khare, B. N., Sagan, C., Arakawa, E. T., et al. 1984, *Icarus*, 60, 127, doi: 10.1016/0019-1035(84)90142-8
- Khare, B. N., Sagan, C., Ogino, H., et al. 1986, *Icarus*, 68, 176, doi: 10.1016/0019-1035(86)90080-1
- Kim, H.-J., Ricardo, A., Illangkoon, H. I., et al. 2011, *Journal of the American Chemical Society*, 133, 9457, doi: 10.1021/ja201769f
- Klippenstein, S. J., & Miller, J. A. 2005, *The Journal of Physical Chemistry A*, 109, 4285
- Kozakis, T., Mendonça, J. M., & Buchhave, L. A. 2022, *Astronomy & Astrophysics*, 665, A156
- Krasnopolsky, V. A. 2009, *Icarus*, 201, 226, doi: 10.1016/j.icarus.2008.12.038
- Kukui, A., Jungkamp, T., & Schindler, R. 1995, *Berichte der Bunsengesellschaft für physikalische Chemie*, 99, 1565
- Kunde, V. G., Aikin, A. C., Hanel, R. A., et al. 1981, *Nature*, 292, 686, doi: 10.1038/292686a0
- Laufer, A., Gardner, E., Kwok, T., & Yung, Y. 1983, *Icarus*, 56, 560
- Lavvas, P. P., Coustenis, A., & Vardavas, I. M. 2008, *Planetary and Space Science*, 56, 27, doi: 10.1016/j.pss.2007.05.026
- Lee, E. K. H., Tsai, S.-M., Hammond, M., & Tan, X. 2023, *Astronomy & Astrophysics*, 672, A110, doi: 10.1051/0004-6361/202245473
- Lellouch, E., Gurwell, M. A., Moreno, R., et al. 2019, *Nature Astronomy*, 3, 614, doi: 10.1038/s41550-019-0749-4
- Linsenmeier, M., Pascale, S., & Lucarini, V. 2015, *Planetary and Space Science*, 105, 43, doi: 10.1016/j.pss.2014.11.003
- Lira-Barria, A., Harvey, J. N., Konings, T., et al. 2024, *Astronomy & Astrophysics*, 692, A158, doi: 10.1051/0004-6361/202452070
- Logan, J. A., Prather, M. J., Wofsy, S. C., & McElroy, M. B. 1981, *Journal of Geophysical Research: Oceans*, 86, 7210, doi: 10.1029/JC086iC08p07210
- Loison, J. C., Hébrard, E., Dobrijevic, M., et al. 2015, *Icarus*, 247, 218, doi: 10.1016/j.icarus.2014.09.039
- Loison, J.-C., Agúndez, M., Wakelam, V., et al. 2017, *MNRAS*, 470, 4075, doi: 10.1093/mnras/stx1265
- Lombardo, N. A., Nixon, C. A., Greathouse, T. K., et al. 2019, *The Astrophysical Journal Letters*, 881, L33, doi: 10.3847/2041-8213/ab3860
- Lora, J. M., Kataria, T., & Gao, P. 2018, *The Astrophysical Journal*, 853, 58, doi: 10.3847/1538-4357/aaa132
- Loyd, R. P., France, K., Youngblood, A., et al. 2016, *The Astrophysical Journal*, 824, 102
- Macpherson, M. T., Pilling, M. J., & Smith, M. J. C. 1983, *Chemical Physics Letters*, 94, 430, doi: 10.1016/0009-2614(83)80761-1
- Madhusudhan, N., Sarkar, S., Constantinou, S., et al. 2023, *The Astrophysical Journal Letters*, 956, L13, doi: 10.3847/2041-8213/acf577
- Mak, M. T., Mayne, N. J., Sergeev, D. E., et al. 2023, 3D simulations of the Archean Earth including photochemical haze profiles, arXiv, doi: 10.48550/arXiv.2310.06818
- Mak, M. T., Sergeev, D. E., Mayne, N., et al. 2024, *Monthly Notices of the Royal Astronomical Society*, 529, 3971, doi: 10.1093/mnras/stae741
- Marston, G., Nesbitt, F. L., Nava, D. F., Payne, W. A., & Stief, L. J. 1989, *The Journal of Physical Chemistry*, 93, 5769, doi: 10.1021/j100352a024
- Marten, A., Gautier, D., Owen, T., et al. 1993, *The Astrophysical Journal*, 406, 285, doi: 10.1086/172440
- Marten, A., Gautier, D., Griffin, M. J., et al. 1995, *Geophysical Research Letters*, 22, 1589, doi: 10.1029/95GL00949
- Massie, S., & Hunten, D. 1981, *Journal of Geophysical Research: Oceans*, 86, 9859
- Miller, S. L. 1953, *Science*, 117, 528, doi: 10.1126/science.117.3046.528
- Miller, S. L., & Schlesinger, G. 1983, *Advances in Space Research*, 3, 47, doi: 10.1016/0273-1177(83)90040-6
- Miller, S. L., & Urey, H. C. 1959, *Science*, 130, 245. <https://www.jstor.org/stable/1757918>
- Miyakawa, S., Yamanashi, H., Kobayashi, K., Cleaves, H. J., & Miller, S. L. 2002, *Proceedings of the National Academy of Sciences*, 99, 14628, doi: 10.1073/pnas.192568299

- Moreno, R., Lellouch, E., Lara, L. M., et al. 2011, *Astronomy & Astrophysics*, 536, L12, doi: 10.1051/0004-6361/201118189
- Moses, J. I., Fouchet, T., Bézard, B., et al. 2005, *Journal of Geophysical Research (Planets)*, 110, E08001, doi: 10.1029/2005JE002411
- Moses, J. I., Visscher, C., Fortney, J. J., et al. 2011, *The Astrophysical Journal*, 737, 15, doi: 10.1088/0004-637X/737/1/15
- Moses, J. I., Marley, M. S., Zahnle, K., et al. 2016, *The Astrophysical Journal*, 829, 66, doi: 10.3847/0004-637X/829/2/66
- Nesbitt, F. L., Marston, G., & Stief, L. J. 1990, *Journal of Physical Chemistry*, 94, 4946
- Nguyen, M. T., Sengupta, D., Vereecken, L., Peeters, J., & Vanquickenborne, L. G. 1996, *The Journal of Physical Chemistry*, 100, 1615, doi: 10.1021/jp9510507
- Nixon, C. A. 2024, *ACS Earth and Space Chemistry*, doi: 10.1021/acsearthspacechem.2c00041
- Oparin, A. I. 1938
- Palmer, M. H., Ballard, C. C., & Walker, I. C. 1999, *Chemical Physics*, 249, 129, doi: 10.1016/S0301-0104(99)00290-6
- Patel, B. H., Percivalle, C., Ritson, D. J., Duffy, C. D., & Sutherland, J. D. 2015, *Nature Chemistry*, 7, 301, doi: 10.1038/nchem.2202
- Pavlov, A. A., Brown, L. L., & Kasting, J. F. 2001, *Journal of Geophysical Research: Planets*, 106, 23267, doi: 10.1029/2000JE001448
- Peacock, S., Barman, T., Shkolnik, E. L., et al. 2020, *The Astrophysical Journal*, 895, 5, doi: 10.3847/1538-4357/ab893a
- Pearce, B. K., Tupper, A. S., Pudritz, R. E., & Higgs, P. G. 2018, *Astrobiology*, 18, 343, doi: 10.1089/ast.2017.1674
- Pearce, B. K. D., Ayers, P. W., & Pudritz, R. E. 2019, *The Journal of Physical Chemistry A*, 123, 1861, doi: 10.1021/acs.jpca.8b11323
- , 2020a, *The Journal of Physical Chemistry A*, 124, 8594, doi: 10.1021/acs.jpca.0c06804
- Pearce, B. K. D., He, C., & Hörst, S. M. 2022a, *ACS Earth and Space Chemistry*, 6, 2385, doi: 10.1021/acsearthspacechem.2c00138
- Pearce, B. K. D., Molaverdikhani, K., Pudritz, R. E., Henning, T., & Cerrillo, K. E. 2022b, *The Astrophysical Journal*, 932, 9, doi: 10.3847/1538-4357/ac47a1
- Pearce, B. K. D., Molaverdikhani, K., Pudritz, R. E., Henning, T., & Hébrard, E. 2020b, *The Astrophysical Journal*, 901, 110, doi: 10.3847/1538-4357/abae5c
- Pearce, B. K. D., Pudritz, R. E., Semenov, D. A., & Henning, T. K. 2017, *Proceedings of the National Academy of Sciences*, 114, 11327, doi: 10.1073/pnas.1710339114
- Pica-Ciamarra, L., Madhusudhan, N., Cooke, G. J., Constantinou, S., & Binet, M. 2025, *A Systematic Search for Trace Molecules in Exoplanet K2-18 b*, arXiv, doi: 10.48550/arXiv.2505.10539
- Poch, O., Coll, P., Buch, A., Ramírez, S. I., & Raulin, F. 2012, *Planetary and Space Science*, 61, 114, doi: 10.1016/j.pss.2011.04.009
- Polino, D., Klippenstein, S. J., Harding, L. B., & Georgievskii, Y. 2013, *The Journal of Physical Chemistry A*, 117, 12677
- Powner, M. W., Anastasi, C., Crowe, M. A., et al. 2007, *ChemBioChem*, 8, 1170
- Powner, M. W., Gerland, B., & Sutherland, J. D. 2009, *Nature*, 459, 239, doi: 10.1038/nature08013
- Prinn, R. G., & Barshay, S. S. 1977, *Science*, 198, 1031, doi: 10.1126/science.198.4321.1031
- Proedrou, E., & Hocke, K. 2016, *Earth, Planets and Space*, 68, 96, doi: 10.1186/s40623-016-0461-x
- Quanz, S. P., Absil, O., Benz, W., et al. 2022, *Experimental Astronomy*, 54, 1197, doi: 10.1007/s10686-021-09791-z
- Ranjan, S., & Sasselov, D. D. 2016, *Astrobiology*, 16, 68, doi: 10.1089/ast.2015.1359
- Ribas, I., Gregg, M. D., Boyajian, T. S., & Bolmont, E. 2017, *Astronomy & Astrophysics*, 603, A58
- Ridgway, R. J., Zamyatina, M., Mayne, N. J., et al. 2023a, *Monthly Notices of the Royal Astronomical Society*, 518, 2472, doi: 10.1093/mnras/stac3105
- , 2023b, *Monthly Notices of the Royal Astronomical Society*, 518, 2472
- Rimmer, P. B. 2023, in *Conflicting Models for the Origin of Life* (John Wiley & Sons, Ltd), 407–424, doi: 10.1002/9781119555568.ch16
- Rimmer, P. B., & Helling, C. 2016, *The Astrophysical Journal Supplement Series*, 224, 9, doi: 10.3847/0067-0049/224/1/9
- Rimmer, P. B., Jordan, S., Constantinou, T., et al. 2021, *The Planetary Science Journal*, 2, 133, doi: 10.3847/PSJ/ac0156
- Rimmer, P. B., & Rugheimer, S. 2019, *Icarus*, 329, 124, doi: 10.1016/j.icarus.2019.02.020
- Rimmer, P. B., Xu, J., Thompson, S. J., et al. 2018, *Science Advances*, 4, eaar3302, doi: 10.1126/sciadv.aar3302
- Ritson, D., & Sutherland, J. D. 2012, *Nature Chemistry*, 4, 895, doi: 10.1038/nchem.1467
- Roscoe, J. M., & Roscoe, S. G. 1973, *Canadian Journal of Chemistry*, 51, 3671, doi: 10.1139/v73-547
- Rosenqvist, J., Lellouch, E., Romani, P. N., Paubert, G., & Encrenaz, T. 1992, *The Astrophysical Journal*, 392, L99, doi: 10.1086/186435
- Ruiz-Mirazo, K., Briones, C., & de la Escosura, A. 2014, *Chemical Reviews*, 114, 285, doi: 10.1021/cr2004844
- Sagan, C., & Chyba, C. 1997, *Science*, 276, 1217, doi: 10.1126/science.276.5316.1217
- Sanchez, R. A., Ferbis, J. P., & Orgel, L. E. 1967, *Journal of Molecular Biology*, 30, 223, doi: 10.1016/S0022-2836(67)80037-8
- Schmidt, S. P., MacDonald, R. J., Tsai, S.-M., et al. 2025, *A Comprehensive Reanalysis of K2-18 b's JWST NIRISS+NIRSpec Transmission Spectrum*, arXiv, doi: 10.48550/arXiv.2501.18477
- Schopf, J. W. 2006, *Elements*, 2, 229, doi: 10.2113/gselements.2.4.229
- Segura, A., Walkowicz, L. M., Meadows, V., Kasting, J., & Hawley, S. 2010, *Astrobiology*, 10, 751, doi: 10.1089/ast.2009.0376
- Sergeev, D. E., Lewis, N. T., Lambert, F. H., et al. 2022, *The Planetary Science Journal*, 3, 214, doi: 10.3847/PSJ/ac83be
- Sergeev, D. E., McDermott, J. W., Woods, L., et al. 2025, *Lightning activity on a tidally locked terrestrial exoplanet in storm-resolving simulations for a range of surface pressures*, arXiv, doi: 10.48550/arXiv.2504.19883
- Shkolnik, E. L., & Barman, T. S. 2014, *The Astronomical Journal*, 148, 64, doi: 10.1088/0004-6256/148/4/64
- Shock, E. L. 1990, *Origins of life and evolution of the biosphere*, 20, 331, doi: 10.1007/BF01808115
- Solé, R. V., & Munteanu, A. 2004, *Europhysics Letters*, 68, 170, doi: 10.1209/epl/i2004-10241-3
- Srinivasan, N. K., Su, M.-C., & Michael, J. V. 2007, *The Journal of Physical Chemistry A*, 111, 3951, doi: 10.1021/jp0673516
- Srinivasan, N. K., Su, M.-C., Sutherland, J. W., & Michael, J. V. 2005, *The Journal of Physical Chemistry A*, 109, 1857, doi: 10.1021/jp040679j
- Strecker, A. 1854, *Justus Liebig's Annalen der Chemie*, 91, 349
- Sutherland, J. D. 2017, *Nature Reviews Chemistry*, 1, 0012, doi: 10.1038/s41570-016-0012
- Taysum, B. M., Palmer, P. I., Olsen, K., et al. 2024, *Astronomy & Astrophysics*, 687, A191, doi: 10.1051/0004-6361/202449546

- Thelen, A. E., Nixon, C. A., Cosentino, R. G., et al. 2022, *The Planetary Science Journal*, 3, 146, doi: 10.3847/PSJ/ac7050
- Thelen, A. E., Nixon, C. A., Chanover, N. J., et al. 2019, *Icarus*, 319, 417, doi: 10.1016/j.icarus.2018.09.023
- Tian, F., Kasting, J. F., & Zahnle, K. 2011, *Earth and Planetary Science Letters*, 308, 417, doi: 10.1016/j.epsl.2011.06.011
- Tomasko, M. G., Doose, L., Engel, S., et al. 2008, *Planetary and Space Science*, 56, 669, doi: 10.1016/j.pss.2007.11.019
- Trainer, M. G., Pavlov, A. A., DeWitt, H. L., et al. 2006, *Proceedings of the National Academy of Sciences*, 103, 18035, doi: 10.1073/pnas.0608561103
- Tsai, S.-M., Innes, H., Wogan, N. F., & Schwieterman, E. W. 2024, *The Astrophysical Journal Letters*, 966, L24, doi: 10.3847/2041-8213/ad3801
- Tsai, S.-M., Kitzmann, D., Lyons, J. R., et al. 2018, *The Astrophysical Journal*, 862, 31, doi: 10.3847/1538-4357/aac834
- Tsai, S.-M., Lee, E. K. H., & Pierrehumbert, R. 2022, *Astronomy & Astrophysics*, 664, A82, doi: 10.1051/0004-6361/202142816
- Tsai, S.-M., Lyons, J. R., Grosheintz, L., et al. 2017, *The Astrophysical Journal Supplement Series*, 228, 20, doi: 10.3847/1538-4365/228/2/20
- Tsai, S.-M., Malik, M., Kitzmann, D., et al. 2021, *The Astrophysical Journal*, 923, 264, doi: 10.3847/1538-4357/ac29bc
- Tsai, S.-M., Lee, E. K. H., Powell, D., et al. 2023, *Nature*, 617, 483, doi: 10.1038/s41586-023-05902-2
- Tsang, W. 1987, *Journal of Physical and Chemical Reference Data*, 16, 471, doi: 10.1063/1.555802
- , 1992, *Journal of Physical and Chemical Reference Data*, 21, 753, doi: 10.1063/1.555914
- Tsang, W., & Hampson, R. 1986, *Journal of physical and chemical reference data*, 15, 1087
- Tsang, W., & Herron, J. T. 1991, *Journal of Physical and Chemical Reference Data*, 20, 609, doi: 10.1063/1.555890
- Turbet, M., Leconte, J., Selsis, F., et al. 2016, *Astronomy & Astrophysics*, 596, A112
- Turbet, M., Fauchez, T. J., Sergeev, D. E., et al. 2022, *The Planetary Science Journal*, 3, 211, doi: 10.3847/PSJ/ac6cf0
- Venot, O., Bounaceur, R., Dobrijevic, M., et al. 2019, *Astronomy & Astrophysics*, 624, A58, doi: 10.1051/0004-6361/201834861
- Venot, O., Hébrard, E., Agúndez, M., Decin, L., & Bounaceur, R. 2015, *Astronomy & Astrophysics*, 577, A33, doi: 10.1051/0004-6361/201425311
- Venot, O., Hébrard, E., Agúndez, M., et al. 2012, *Astronomy & Astrophysics*, 546, A43, doi: 10.1051/0004-6361/201219310
- Vida, K., Oláh, K., Kóvári, Z., et al. 2019, *The Astrophysical Journal*, 884, 160, doi: 10.3847/1538-4357/ab41f5
- Visscher, C., Moses, J. I., & Saslow, S. A. 2010, *Icarus*, 209, 602, doi: 10.1016/j.icarus.2010.03.029
- Vuitton, V., Yelle, R. V., Klippenstein, S. J., Hörst, S. M., & Lavvas, P. 2019, *Icarus*, 324, 120, doi: 10.1016/j.icarus.2018.06.013
- Wang, H., & Frenklach, M. 1997, *Combustion and Flame*, 110, 173, doi: 10.1016/S0010-2180(97)00068-0
- Welbanks, L., Nixon, M. C., McGill, P., et al. 2025, *The Challenges of Detecting Gases in Exoplanet Atmospheres*, arXiv, doi: 10.48550/arXiv.2504.21788
- Westmoreland, P. R., Dean, A. M., Howard, J. B., & Longwell, J. P. 1989, *The Journal of Physical Chemistry*, 93, 8171
- White, S. B., & Rimmer, P. B. 2025, *Accounts of Chemical Research*, 58, 1, doi: 10.1021/acs.accounts.4c00247
- Willacy, K., Allen, M., & Yung, Y. 2016, *The Astrophysical Journal*, 829, 79, doi: 10.3847/0004-637X/829/2/79
- Wilson, D. J., Froning, C. S., Duvvuri, G. M., et al. 2021, *The Astrophysical Journal*, 911, 18, doi: 10.3847/1538-4357/abe771
- , 2024, *The Astrophysical Journal*, 978, 85, doi: 10.3847/1538-4357/ad9251
- Winberg, F. A. F., Kreidberg, L., Moses, J. I., Percival, C. J., & Palmer, P. I. 2025, *Nature*, 646, 1057, doi: 10.1038/d41586-025-03478-7
- Wolf, E. T., & Toon, O. B. 2010, *Science*, 328, 1266, doi: 10.1126/science.1183260
- Wong, M. L., Prabhu, A., Williams, J., Morrison, S. M., & Hazen, R. M. 2023, *Journal of Geophysical Research: Planets*, 128, e2022JE007658, doi: 10.1029/2022JE007658
- Xu, J., J. Ritson, D., Ranjan, S., et al. 2018, *Chemical Communications*, 54, 5566, doi: 10.1039/C8CC01499J
- Yates, J. S., Palmer, P. I., Manners, J., et al. 2020, *Monthly Notices of the Royal Astronomical Society*, 492, 1691, doi: 10.1093/mnras/stz3520
- Yoshida, T., Koyama, S., Nakamura, Y., Terada, N., & Kuramoto, K. 2024, *Astrobiology*, 24, 1074, doi: 10.1089/ast.2024.0048
- Youngblood, A., France, K., Loyd, R. P., et al. 2016, *The Astrophysical Journal*, 824, 101
- Yu, T., Yang, D. L., & Lin, M. C. 1993, *International Journal of Chemical Kinetics*, 25, 1053, doi: 10.1002/kin.550251210
- Yung, Y. L., Allen, M., & Pinto, J. P. 1984, *The Astrophysical Journal Supplement Series*, 55, 465, doi: 10.1086/190963
- Zahnle, K., Arndt, N., Cockell, C., et al. 2007, *Space Science Reviews*, 129, 35, doi: 10.1007/s11214-007-9225-z
- Zahnle, K., Marley, M. S., Freedman, R. S., Lodders, K., & Forney, J. J. 2009, *The Astrophysical Journal*, 701, L20, doi: 10.1088/0004-637X/701/1/L20
- Zahnle, K., Marley, M. S., Morley, C. V., & Moses, J. I. 2016, *The Astrophysical Journal*, 824, 137, doi: 10.3847/0004-637X/824/2/137
- Zahnle, K. J. 1986, *Journal of Geophysical Research: Atmospheres*, 91, 2819, doi: 10.1029/JD091iD02p02819
- Zahnle, K. J., & Marley, M. S. 2014, *The Astrophysical Journal*, 797, 41, doi: 10.1088/0004-637X/797/1/41